Parameter Estimation
for Time-Selective Fading Channels and
Multibeam Satellite Links

MASTER THESIS

Dipl.-Ing. Dr.techn. Michael Bergmann

Supervisor: Ass. Prof. Dipl.-Ing. Dr.techn. Univ.-Doz. Wilfried Gappmair

Institute of Communication Networks and Satellite Communications

Graz University of Technology

Austria

January 2014

"All truths are easy to understand once discovered;
the point is to discover them"

(Galileo Galilei)

"To know that we know what we know,
and to know that we do not know what we do not know,
that is true knowledge"

(Nicolaus Copernicus)

STATUTORY DECLARATION

I hereby declare that I have authored this master thesis independently, that I have not used other than the revealed sources / resources and that I have explicitly marked all material which has been quoted either literally or by content from the used sources.

Graz, January 25th, 2014   ………………………………………….
                                        (Dipl.-Ing. Dr.techn. Michael Bergmann)

to my family

ACKNOWLEDGEMENTS

ABSTRACT

Transferring information efficiently is the Holy Grail in the realm of communications, which especially holds true for wireless systems since licensed bandwidth is expensive. To exploit the latter efficiently, accurate knowledge about the current link conditions is mandatory demanding smart parameter estimation methods. In this respect, this thesis follows up on the dissertation published by the author discussing channel estimations on mobile satellite channels and on multibeam satellite links.

Mobile satellite links are modelled as Rice channels in this work; according to recent advances in this topic, a broader theoretical analysis is presented, delivering maximum likelihood estimators for the power parameters and power ratios presuming knowledge of the Doppler spread and the angle of signal arrival. It will be demonstrated that for most of the estimated parameters the theoretical performance limits can be met. The presented work also holds true for general mobile links following a Rayleigh distribution with line-of-sight component.

Multibeam satellite links are of major concern of current research activities as they are an enabler technology to boost the throughput in the coverage region of a satellite at no extra cost for licensed bandwidth. Given aggressive frequency reuse strategies, interference is a major hurdle to tackle; algorithms mitigating the latter again require accurate channel estimations. For the latter this thesis presents and analyses a novel estimation concept which outperforms current ones, thus Graz University of Technology decided to preserve all rights of use for this technology and triggered a patent filing.

ZUSAMMENFASSUNG

Effiziente Informationsübertragung ist der Heilige Gral im Design von Kommunikationssystemen, was speziell für Freiraumübertragungssysteme gilt, da lizensierte Frequenzbänder sehr teure Ressourcen sind. Um letztere daher besser auszunutzen, ist eine genaue Kanalschätzung notwendig, die die aktuellen Bedingungen am Link entsprechend abbildet. In diesem Zusammenhang versteht sich diese Arbeit als Erweiterung der vom Autor veröffentlichten Dissertation, welche Kanalparameterschätzungen auf mobilen Satellitenkanälen und auf Multibeam-Satellitenkanälen zum Thema hat.

Mobile Satellitenkanäle werden hier als Rice-Kanäle modelliert. Basierend auf bereits veröffentlichten Arbeiten, wurden Maximum-Likelihood Schätzer für Leistungsparameter und Leistungsverhältnisse entwickelt, welche als Grundlage das Wissen über die vorhandene Doppler-Spreizung und den Empfangswinkel des Signals voraussetzen. Anhand von Simulationen wird gezeigt, dass die Schätzgenauigkeit für die meisten Parameter an der theoretischen Grenze liegt. Die präsentierten Analysen sind generell für Kanäle gültig, die einer Rayleigh-Verteilung in Kombination mit einer direkten Signalkomponente entsprechen.

Multibeam-Satellitenkanäle sind ein brandaktuelles Forschungsgebiet, da sie als Schlüsseltechnologie gelten, um den zukünftigen erhöhten Datendurchsatz im Versorgungsgebiet eines Satelliten zu gewährleisten, ohne in zusätzliche lizensierte Bandbreite investieren zu müssen. Dazu sind ambitionierte Frequenz-Wiederverwendungsstrategien notwendig, die jedoch gewaltige Interferenzprobleme aufwerfen. Letztere können durch passende Algorithmen vermindert werden, diese benötigen aber genaue Kanalschätzungen. Diese Arbeit stellt in diesem Zusammenhang ein völlig neues Schätzkonzept vor, welches auf Grund seiner hervorragenden Leistungseigenschaften von der Technischen Universität Graz zur Patentierung ausgewählt wurde, um sich alle Verwertungsrechte zu sichern.

CONTENTS

LIST OF FIGURES

1 Introduction

This thesis follows up on the dissertation the author published in [1]; recent advances in the topics discussed therein inspired this master thesis. Therefore the work presented throughout this thesis is split into two main chapters: Chapter 2 discusses the advances made in parameter estimations on time-selective and frequency-flat fading channels and Chapter 3 presents the advances made in parameter estimations on multibeam satellite channels. The latter led to a novel technology triggering a patent filing process by Graz University of Technology.

Mobile channels are a major subject in current research activities on satellite communications. Subject to this thesis therefore is in the extension of the work recently published in [1]-[6] focusing on parameter estimations by mathematical advances made in [7] and [8]. Parameter estimation is a key technology when appropriately employed to foster the exploitation of the available link capacity. Hence, appropriate figures of merit such as the signal, noise and interference powers, or more prominently their ratios are of pivotal interest and as such subject to estimation. Considering perfect symbol timing, this task requires carrier frequency and phase recovery, Doppler spread estimation and finally the estimation of the power parameters. In this context the analytical work in [7] and [8] is introduced and two parameter estimators, i.e. a nonlinear one and a linearized one, which mainly operate in the spectral domain, are examined and their performances are analysed.

Also multibeam satellite links are of major concern of research activities, as current calls emitted by the European Space Agency (ESA) indicate. Those architectures split the service region of a communication satellite into several cells, which in novel concepts foresee aggressive frequency reuse strategies (up to full frequency reuse). Not surprisingly, high levels of interference are the consequences of such aggressive frequency reuse policies, which – to prevent the throughput from outage – require accurate channel estimations. Following on the activities pursued by the author in the context of the ESA SatNEx III project, which were extensively discussed in [1], a novel estimation concept is introduced employing the knowledge of the user terminal position and the multibeam antenna pattern in a different way compared to [1] and related follow-up publications. This novel method performs much better, such that for a given training sequence the estimation error is much smaller or, alternatively, that certain estimation accuracies can be achieved with significantly shorter training sequences. Due to the significantly improved performance, a patent filing process was initiated.

2   Parameter Estimation on Rician Fading Channels

The investigations carried out in this chapter was motivated by results from predecessor work published in [1]-[6] on land mobile satellite links modelled as frequency-flat and time-selective correlated Rician fading channels; in addition, it is based on the advances made in [7][8], which also provides the necessary mathematical inputs for this thesis. It shall be emphasized that this thesis refers to a more general approach compared to the predecessor studies, such that it might be considered as an extension of the research work done so far. However, the scenario presented here requires similar basics as put down in the author's Dissertation [1]; therefore, important aspects of this thesis are repeatedly mentioned in this work, where necessary, to support the logical flow and the readability.

Within the following, after some introductory words in Section 2.1, Sections 2.2 and 2.3 explain the Rice channel and the applied signal model. In Section 2.4 the estimation framework is introduced, Section 2.5 considers the relevant performance limits and Sections 2.6 and 2.7 present simulation results and investigations on estimator stability. Section 2.8 concludes the main aspects of the work carried out in this chapter.

2.1   Preface

Awareness of channel conditions is indispensable for many communication systems to maintain reliability and efficiency by adapting the transmission schemes accordingly. To this end appropriate estimation strategies must be found, ideally performing close to a theoretical limit, which is given by the so called *Cramer-Rao lower bound* (CRLB) [9, p. 4][10].

As mentioned before, adaptive transmission scenarios, typically implemented as *adaptive coding and modulation* (ACM) schemes are capable to meet the capacity limit of a fading channel, but they require timely and accurate information about the channel, usually denoted as *channel state information* (CSI) [12]. Traditional ACM concepts typically refer to the signal-to-noise ratio (SNR) as the principal figure of merit, which is widely sufficient when the channel conditions do not vary significantly within the *round-trip time* (RTT) of the link. However, advanced ACM schemes for fast fading channels, which are typical to mobile scenarios, might require information beyond that [13][14]; such schemes normally demand information about the power factors as well as their ratios, i.e., the *signal-to-noise plus interference ratio* (SNIR), the *signal-to-*

interference ratio (SIR) (also denoted as Rice Factor), the Doppler spread and other higher layer performance parameters (e.g. bit/packet/frame error rate) [15].

2.2 The Rician Channel

The Rician channel is composed of Rayleigh distributed multipath components, which are responsible for fading effects, and a *line-of-sight* (LoS) component [16], thus it representatively models different types of practical communication links. Figure 2.1 exemplifies a satellite forward link, where both sender and receiver move at different speed. The blue arrow indicates the path of the LoS component and the green ones represent the multipath components, which constructively and destructively add up at the receiver in the mobile *user terminal* (UT).
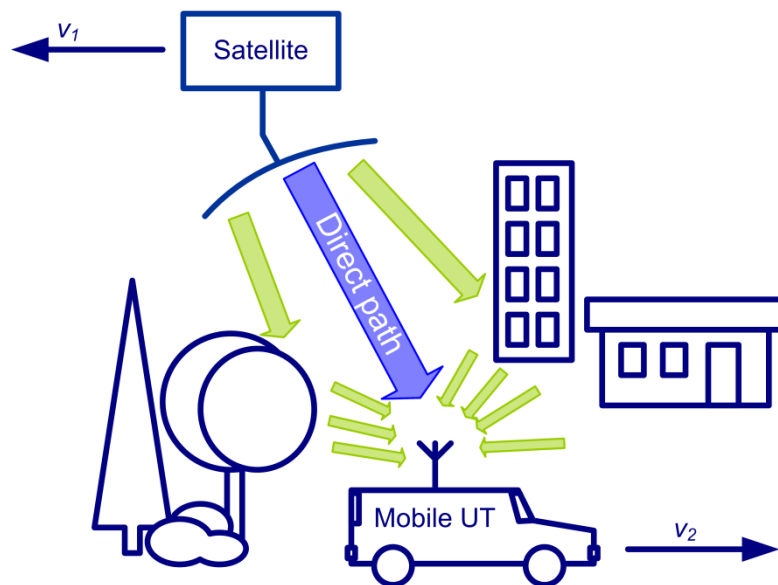
Figure 2.1: Example scenario for a Rice Channel

Given the sketched spectrum of the Rice channel in Figure 2.2 and the exemplified scenario, it becomes clear that the Doppler spread B_μ, which represents the span of the interference (fading) component (green) in the power spectrum, basically results from the UT speed v_2, whereas Δf_c represents the Doppler shift of the LoS component (blue) originating from the relative velocity between sender and receiver and inaccuracies of the local oscillators; f_α results from the incidence angle of the LoS component. *Additive white Gaussian noise* (AWGN) is also present and indicated in red.

A closer inspection of the power spectrum will be provided in the following discussing its characteristics as well as the signal model for estimations in due detail.
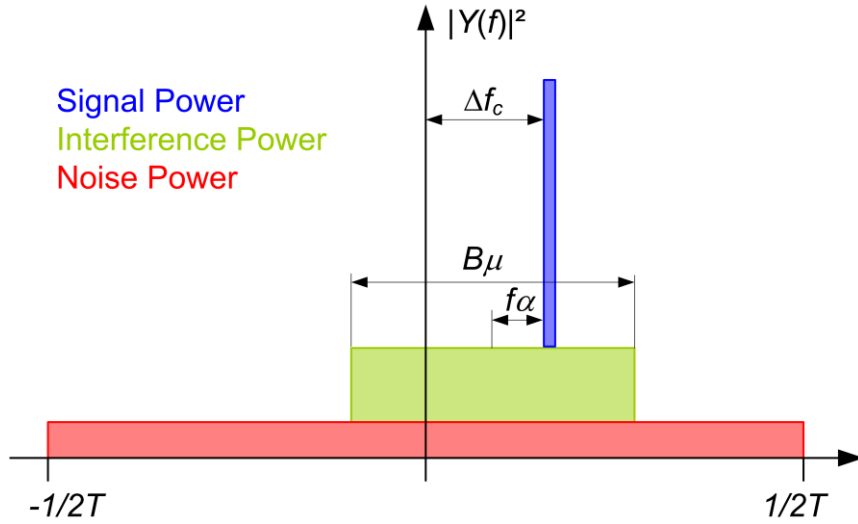
Figure 2.2: Sketched power spectrum of the Rice channel

2.2.1 Coherence Time and Doppler Spread

As mentioned before, the Rice channel, as considered, is frequency-flat and time-selectively correlated, which is a valid approach for narrowband systems. The maximum *Doppler spread* B_μ and the *coherence time* T_μ, respectively, are important characteristics in that respect. The latter measures the period the fading components are mutually correlated. This yields for the exemplified scenario

$$f_\mu = \frac{v_2}{\lambda_c} = \frac{B_\mu}{2}, \tag{2.1}$$

where v_2 represents the velocity of the mobile UT, λ_c denotes the carrier wavelength, and T_μ is given by [17][18][19, pp. 16-17]

$$T_\mu \cong \frac{1}{f_\mu}. \tag{2.2}$$

2.2.2 Angle of Arrival of the Signal Component

As mentioned before, f_α is a function of the *angle of arrival* (AoA) of the signal component:

$$f_\alpha = f_\mu \cdot cos(\alpha), \tag{2.3}$$

where α represents the incidence angle (= AoA) of the LoS component measured counter-clockwise with respect to the velocity vector of the mobile *receiver* (Rx). Figure 2.3 depicts this behaviour; the receive spectra of different AoAs are exemplified which, however, are plotted at the *transmitter* (Tx) side for a clearer interpretability. The green-ish area around Rx indicates the scatter environment. It can clearly be seen that the signal component moves within the Doppler spread according to the AoA.
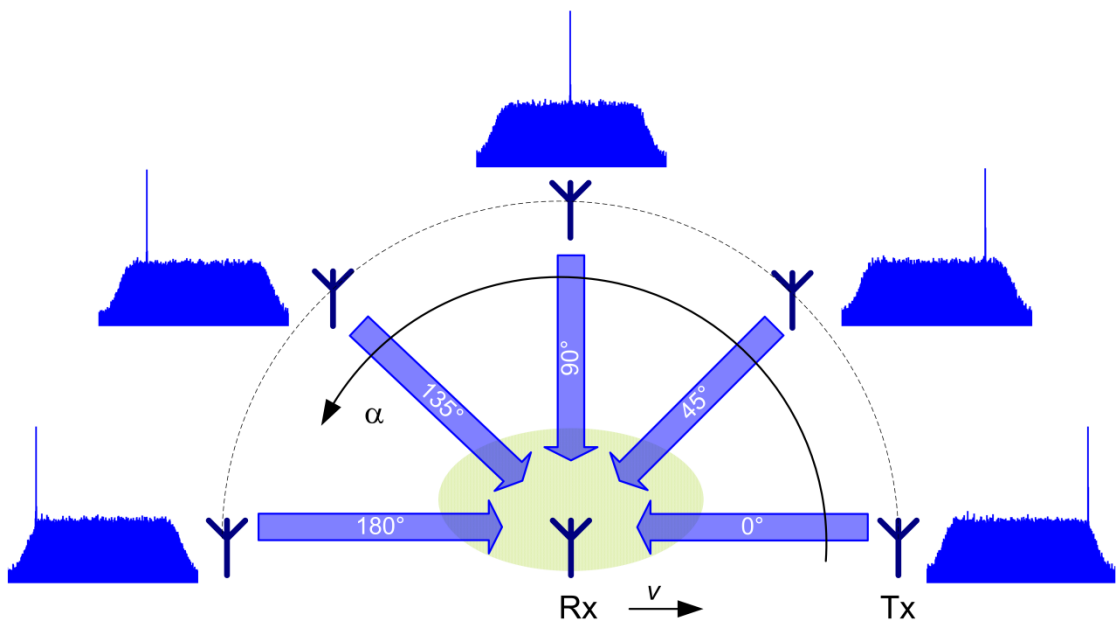
Figure 2.3: Impact of the AoA on the power spectrum

2.2.3 Spectral Shape of the Fading Component

The fading component can have different shapes which depend on the scattering model applied. The Jakes model, which describes isotropic scattering, or scatter models with near-rectangular spectral shapes are often used in literature; the latter is suggested for satellite channels [1][17][18]. Eventually, the exact shape of the spectrum is regarded less important than the Doppler spread [20][2, p. 38].

Figure 2.4 [1] depicts the *power spectral density* (PSD) of the Rice channel with the multipath component implemented as a Jakes filter model realized as a 201 tapped *finite impulse response* (FIR) *low pass filter* (LPF); the incident angle of the direct path signal is considered to be zero degrees. The theoretical PSD is given by

$$S_\mu(f) = \frac{1}{\pi \cdot f_\mu \cdot \sqrt{1 - f^2/f_\mu^2}} \ , |f| \leq f_\mu, \tag{2.4}$$

where $S_\mu(f) = 0$, when $f > f_\mu$ [18].

Figure 2.5 [1] depicts the PSD of a Rice channel with a 10th order Butterworth filter implementing the multipath component; again, the incident angle of the direct path signal is considered to be zero degrees. The theoretical PSD is given by

$$S_\mu(f) = \frac{1}{1 + (f/f_\mu)^{2p}}, \tag{2.5}$$

where p denotes the number of poles [9, p. 247].
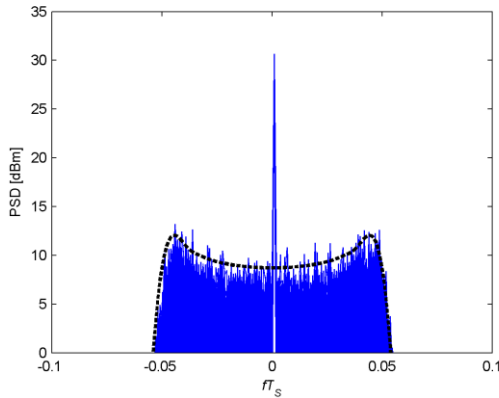
Figure 2.4: Jakes filter implementation of the multipath component
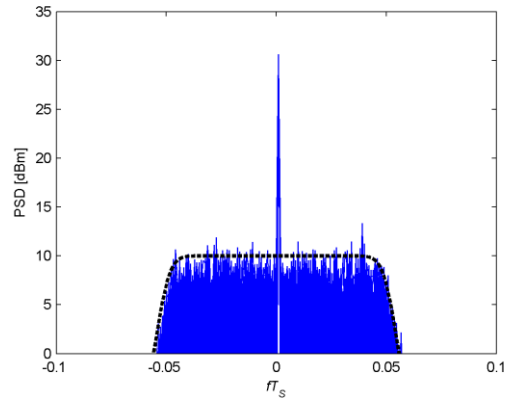
Figure 2.5: Butterworth filter implementation of the multipath component

It is to be noticed that later on Jakes and Butterworth filter implementations are also referred to as isotropic and non-isotropic scatter model, respectively, although the implementation as 201 tapped FIR Jakes filter may not anymore be regarded as isotropic in the strict sense of the meaning as it only loosely approximates (2.4).

2.3 Signal Model

After having the main elements of a Rice channel introduced, the baseband signal model can be established. In analogy to Figure 2.6 the received signal furnishes to

$$r_k = \left(a \cdot e^{j\theta} + \mu_k\right) \cdot e^{j2\pi k \nu} \cdot c_k + w_k \,, \tag{2.6}$$

where a and θ represent the amplitude and the phase offset of the signal component, respectively, ν is the by the symbol period T normalized frequency error, c_k is the k-th symbol transmitted, and $w_k \sim \mathcal{N}_c(0, 2\sigma_w^2)$ is a circular-complex zero mean white Gaussian noise process also denoted as AWGN, which yields $E[w_i^* \cdot w_j] = 2\sigma_w^2 \cdot \delta_{ij}$, where $E[\cdot]$ stands for expectation. Furthermore, the interference component μ_k is derived from $s_\mu(t) = \mathcal{F}^{-1}\left(S_\mu(f - f_\alpha)\right)$, where $\mathcal{F}^{-1}$ denotes the inverse Fourier transform. Having $s_k = s_\mu(k \cdot T_s)$, where T_S is the sampling period, and $u_k = u_{k,i} + j \cdot u_{k,q}$, $u_k \sim \mathcal{N}_c(0, 2\sigma_u^2)$, it follows that μ_k is the k-th element of

$$\boldsymbol{\mu} = \mathbf{s} * \mathbf{u}, \tag{2.7}$$

where "$*$" stands for convolution[1]. This yields $\mu_k \sim \mathcal{N}_c\left(0, 2\sigma_\mu^2\right) = \mathcal{N}_c(0, 2\sigma_u^2 \cdot \mathbf{s}^H \mathbf{s})$ with the superscript "H" indicating the Hermitian. The expectation gives $E[\mu_k^* \cdot \mu_{k+i-j}] = E[\mu_k^* \cdot \mu_{k-i+j}] = 2\sigma_\mu^2 [\mathbf{C}_\mu]_{ij}$, $[\mathbf{C}_\mu]_{ii} = 1$, where $\mathbf{C}_\mu$ denotes the covariance matrix[2] [7].
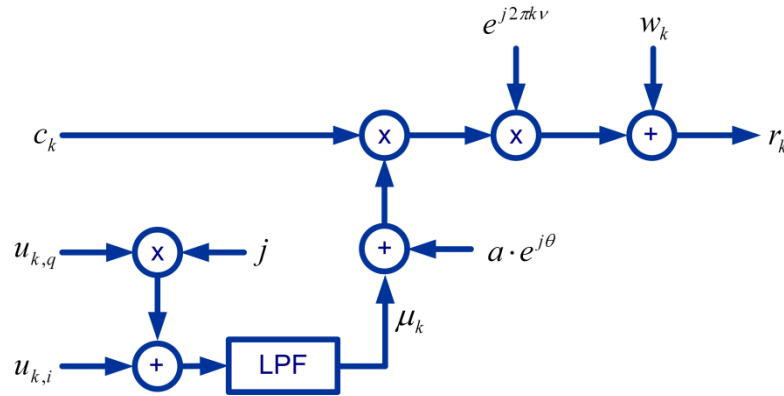
Figure 2.6: Rice channel signal model

---

[1] For simulations, transient effects of the filter upon initialisation have to be considered. Thus the filter has to be loaded with a number of circular-complex Gaussian random samples equalling the number of taps before using the filter output signal. Otherwise, the fading process can also be modelled as an autoregressive process in a recursive function as described in [20].

[2] It is suggested to normalize the filter output power for simulations such that $\mathbf{s}^H \mathbf{s} = 1$.

Since estimations are foreseen as *data-aided* (DA), the data modulation can be removed by

$$z_k = c_k^* \cdot r_k = \left(a \cdot e^{j\theta} + \mu_k\right) \cdot e^{j2\pi k\nu} \cdot |c_k|^2 + c_k^* \cdot w_k \,. \tag{2.8}$$

Considering $|c_k| = 1$ and $c_k^* \cdot w_k = w_k' \sim w_k$, i.e., w_k and w_k' exhibit the same statistical properties ,(2.8) can be rewritten as

$$z_k = \left(a \cdot e^{j\theta} + \mu_k\right) \cdot e^{j2\pi k\nu} + w_k' \,. \tag{2.9}$$

From (2.9) the SNR and the SIR can be established as

$$\rho = \frac{S}{N} = \frac{a^2}{2\sigma_w^2} \tag{2.10}$$

and

$$K_R = \frac{S}{I} = \frac{a^2}{2\sigma_\mu^2}, \tag{2.11}$$

respectively, noting that the signal power $S = a^2$, the noise power $N = 2\sigma_w^2$ and the interference power $I = 2\sigma_\mu^2$ [7].

2.4 Data-Aided Maximum-Likelihood Estimation

Given the signal model, it is clear that the parameter vector to be estimated consists of carrier and power parameters, i.e., $\mathbf{q} = (q_1, q_2, q_3, q_4, q_5) = (\nu, \theta, S, I, N)$. As already mentioned, estimations are considered to be DA, thus training sequences (also preambles or unique words) are agreed between Tx and Rx in the physical layer framing structure. This means that the receiver has *a priori* knowledge of the transmitted training data, thus the parameter vector to be estimated is achieved from an observed sequence of L symbols, i.e., $\mathbf{z} = (z_0, z_1, ..., z_{L-1})^T$, where T denotes the transpose. With $S = a^2$,

$\mu_k \cdot e^{j2\pi k\nu} = \sqrt{I} \cdot \eta_k$, $\eta_k \sim \mathcal{N}_c(0,1)$, and $c_k^* \cdot w_k' = \sqrt{N} \cdot n_k$, $n_k \sim \mathcal{N}_c(0,1)$, (2.9) can be written as

$$z_k = \sqrt{S} \cdot e^{j(2\pi k\nu + \theta)} + \sqrt{I} \cdot \eta_k + \sqrt{N} \cdot n_k, \tag{2.12}$$

which in vector notation yields

$$\mathbf{z} = \mathbf{m} + \sqrt{I} \cdot \boldsymbol{\eta} + \sqrt{N} \cdot \mathbf{n} \tag{2.13}$$

where $\mathbf{m} = \sqrt{S} \cdot e^{j\theta} \cdot \left(1, e^{j2\pi\nu}, e^{j4\pi\nu}, \dots, e^{j2\pi(L-1)\nu}\right)^T$ and $\boldsymbol{\eta}$ and $\mathbf{n}$ represent fading and noise, respectively [7][8].

To arrive at a DA maximum-likelihood (ML) estimator, the probability function for $\mathbf{z}$ must be available. From (2.12) it is obvious that z_k is a realisation of a Gaussian process determined by the mutually independent noise and fading processes; it is to be recalled that the latter is bandlimited. Knowing that the probability function can be established as [24][8]

$$\Pr(\mathbf{z}) = \frac{1}{\pi^L \cdot \det(\mathbf{Q})} \cdot \exp\left(-(\mathbf{z} - \mathbf{m})^H \cdot \mathbf{Q}^{-1} \cdot (\mathbf{z} - \mathbf{m})\right), \tag{2.14}$$

where H denotes the Hermitian transpose and $\mathbf{Q}$ represents the covariance matrix of $\mathbf{z}$ obtained as

$$\mathbf{Q} = E[(\mathbf{z} - \mathbf{m}) \cdot (\mathbf{z} - \mathbf{m})^H] = I \cdot E[\boldsymbol{\eta} \cdot \boldsymbol{\eta}^H] + N \cdot E[\mathbf{n} \cdot \mathbf{n}^H]. \tag{2.15}$$

With $\mathbf{C}_\mu = E[\boldsymbol{\eta} \cdot \boldsymbol{\eta}^H]$ and $\mathbf{I}_L = E[\mathbf{n} \cdot \mathbf{n}^H]$, where $\mathbf{I}_L$ represents the L-dimensional identity matrix, (2.15) can be rewritten as

$$\mathbf{Q} = I \cdot \mathbf{C}_\mu + N \cdot \mathbf{I}_L. \tag{2.16}$$

When considering the tractability of the *log-likelihood function* (LLF) $\Lambda = \log \Pr(\mathbf{z})$, $\mathbf{C}_\mu$ can be approximated by its circular shape [20] assuming that the observation length

L is much larger than the correlation length L_μ of the fading process; the latter results from the product of coherence time T_μ and the baud rate $1/T$. However, in this case $\mathbf{C}_\mu$ decomposes into

$$\mathbf{C}_\mu = \mathbf{V}^H \cdot \boldsymbol{\Sigma}_\mu \cdot \mathbf{V}, \tag{2.17}$$

where $\mathbf{V}^H \cdot \mathbf{V} = \mathbf{I}_L$, $\mathbf{V} = (\mathbf{v}_0, \mathbf{v}_1, \dots, \mathbf{v}_{L-1})$, of which each $\mathbf{v}_k = L^{-1/2}\big(1, e^{j2\pi k/L},$ $e^{j4\pi k/L} \dots, e^{j2\pi k(L-1)/L}\big)^T$, $k = 0,1,\dots,L-1$; furthermore, $\boldsymbol{\Sigma}_\mu$ is an L-dimensional diagonal matrix whose entries λ_k are the result of the *discrete Fourier transform* (DFT) of the fading component, i.e., $\lambda_k = S_\mu\big((f - f_\alpha) \cdot k \cdot T_s\big)$, and represent the eigenvalues of $\mathbf{C}_\mu$ [7][7][8].

By substituting (2.16) and (2.17) into the LLF of (2.14), then, by omitting constants and immaterial factors it is

$$\Lambda = -\log\big(\det[\mathbf{V}^H(N\mathbf{I} + I\boldsymbol{\Sigma}_\mu)\mathbf{V}]\big) - \mathbf{z}^H\mathbf{V}^H(N\mathbf{I} + I\boldsymbol{\Sigma}_\mu)^{-1}\mathbf{V}\mathbf{z}$$
$$+2\mathrm{Re}\left[\mathbf{m}^H\mathbf{V}^H(N\mathbf{I} + I\boldsymbol{\Sigma}_\mu)^{-1}\mathbf{V}\mathbf{z}\right] - \mathbf{m}^H\mathbf{V}^H(N\mathbf{I} + I\boldsymbol{\Sigma}_\mu)^{-1}\mathbf{V}\mathbf{m}. \tag{2.18}$$

With $\boldsymbol{\zeta} = \mathbf{V} \cdot \mathbf{z}$ and $\zeta_i = [\mathbf{V} \cdot \mathbf{z}]_i = \frac{1}{\sqrt{L}} \cdot \sum_{k=0}^{L-1} e^{j2\pi ik/L} \cdot z_k$, which represents the DFT of $\mathbf{z}$, and with $\boldsymbol{\mu} = \mathbf{V} \cdot \big(1, e^{j2\pi v}, e^{j4\pi v}, \dots, e^{j2\pi(L-1)v}\big)^T$ such that $\mathbf{V} \cdot \mathbf{m} = \sqrt{S} \cdot e^{j\theta} \cdot \boldsymbol{\mu}$, the LFF adapts to

$$\Lambda = -\log\big(\det[(N\mathbf{I} + I\boldsymbol{\Sigma}_\mu)]\big) - \boldsymbol{\zeta}^H(N\mathbf{I} + I\boldsymbol{\Sigma}_\mu)^{-1}\boldsymbol{\zeta}$$
$$+2\sqrt{S}\mathrm{Re}\left[e^{-j\theta}\boldsymbol{\mu}^H(N\mathbf{I} + I\boldsymbol{\Sigma}_\mu)^{-1}\boldsymbol{\zeta}\right] - S\boldsymbol{\mu}^H(N\mathbf{I} + I\boldsymbol{\Sigma}_\mu)^{-1}\boldsymbol{\mu}, \tag{2.19}$$

which after some algebra results in [8]

$$\Lambda = \sum_{k=0}^{L-1}\left(\log\frac{1}{N + \lambda_k I} - \frac{|\zeta_k|^2 - 2\sqrt{S}\mathrm{Re}\big[e^{-j\theta}\mu_k^*\zeta_k\big] + S|\mu_k|^2}{N + \lambda_k I}\right). \tag{2.20}$$

From (2.20) an ML estimator can straightforwardly be obtained by establishing the first derivative with respect to the estimation parameter q_i and equating this to zero. Doing this for the parameter vector $\mathbf{q}$ and considering $\mathbf{\mu}' = \partial\mathbf{\mu}/\partial\nu = j2\pi\mathbf{V} \cdot \left(0, e^{j2\pi\nu}, 2e^{j4\pi\nu}, \dots, (L-1)e^{j2\pi(L-1)\nu}\right)^T$ results in the following relationships [7][8]:

$$t_1 = \frac{\partial\Lambda}{\partial\theta} = \sum_{k=0}^{L-1} \frac{2\sqrt{S} \cdot \text{Im}\left[e^{-j\theta} \cdot \mu_k^*\zeta_k\right]}{N + \lambda_k \cdot I} = 0, \tag{2.21}$$

$$t_2 = \frac{\partial\Lambda}{\partial\nu} = \sum_{k=0}^{L-1} \frac{2\sqrt{S} \cdot \text{Re}\left[e^{-j\theta} \cdot (\mu_k')^*\zeta_k\right] - 2S\text{Re}[\mu_k'\mu_k^*]}{N + \lambda_k \cdot I} = 0, \tag{2.22}$$

$$t_3 = \frac{\partial\Lambda}{\partial S} = \sum_{k=0}^{L-1} \frac{\text{Re}\left[e^{-j\theta} \cdot \mu_k^*\zeta_k\right] - \sqrt{S}|\mu_k|^2}{\sqrt{S}(N + \lambda_k \cdot I)} = 0, \tag{2.23}$$

$$t_4 = \frac{\partial\Lambda}{\partial N} = \sum_{k=0}^{L-1} \left(-\frac{1}{N + \lambda_k \cdot I} \right.$$
$$\left. + \frac{|\zeta_k|^2 - 2\sqrt{S} \cdot \text{Re}\left[e^{-j\theta} \cdot \mu_k^*\zeta_k\right] + S|\mu_k|^2}{(N + \lambda_k \cdot I)^2}\right) = 0, \tag{2.24}$$

$$t_5 = \frac{\partial\Lambda}{\partial I} = \sum_{k=0}^{L-1} \left(-\frac{\lambda_k}{N + \lambda_k \cdot I} \right.$$
$$\left. + \lambda_k \frac{|\zeta_k|^2 - 2\sqrt{S} \cdot \text{Re}\left[e^{-j\theta} \cdot \mu_k^*\zeta_k\right] + S|\mu_k|^2}{(N + \lambda_k \cdot I)^2}\right) = 0. \tag{2.25}$$

By detailed inspection of (2.21)-(2.25) it becomes clear that no closed form solution is available, thus requiring a numerical approximation, e.g. the Newton-Raphson algorithm [25, pp. 362-368]. This approach is typically very sensitive to the initialization which possibly causes stability and convergence problems; in that particular case, such issues predominantly arise for the initialization of the frequency offset ν; this can be tackled by treating this parameter separately via appropriate means such as those published in [21]-[23] [8].

2.4.1 Estimations with Negligible Frequency Error

Considering frequency correction by an appropriate and powerful method, e.g. the Mengali-Morelli [21], the Luise-Regiannini [22], or the Rife-Boorstyn [23] algorithms,

the residual frequency error may be regarded negligible, i.e. $\Delta v = v - \hat{v} \to 0$. There-fore, (2.12) may be modified to

$$z_k = \sqrt{S} \cdot e^{j\theta} + \sqrt{I} \cdot \eta_k + \sqrt{N} \cdot n_k \tag{2.26}$$

represented by the vector diagram in Figure 2.7 [7][1, pp. 109-110] and its spectrum is sketched in Figure 2.8.
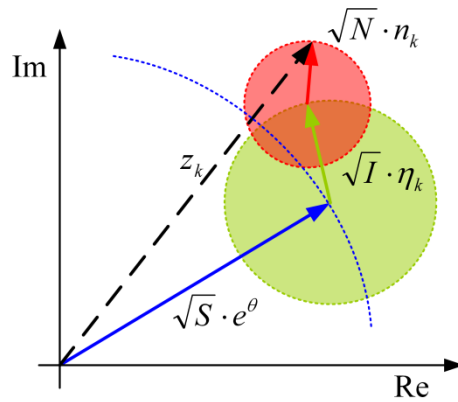
Figure 2.7: Vector diagram for the Rice Channel
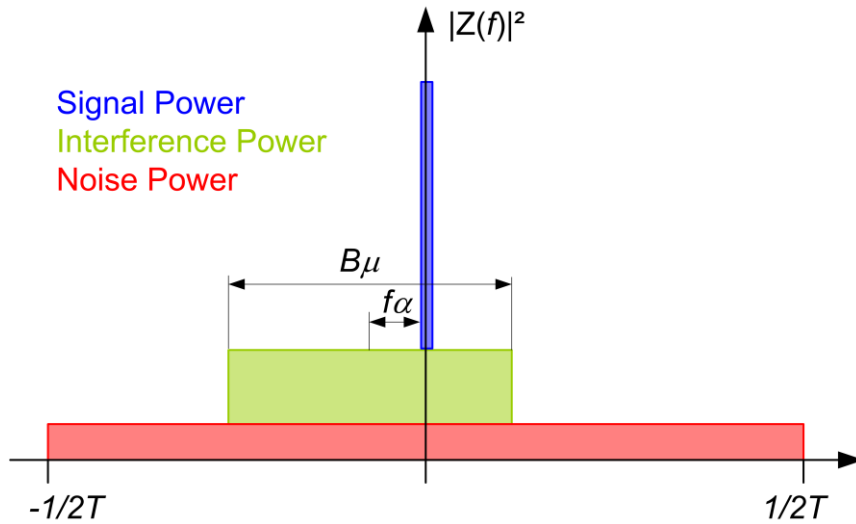
Figure 2.8: Sketched power spectrum of the Rice channel
after frequency correction

Analogous to (2.12), (2.26) can be written in vector notation as

$$\mathbf{z} = \mathbf{m} + \sqrt{I} \cdot \boldsymbol{\eta} + \sqrt{N} \cdot \mathbf{n}, \tag{2.27}$$

resulting in an LLF as represented in (2.20). For this case, however, $\mathbf{m} = \sqrt{S} \cdot e^{j\theta} \cdot \mathbf{1}_L^T$, where $\mathbf{1}_L$ indicates a vector of L ones and $\boldsymbol{\mu} = \mathbf{V} \cdot \mathbf{1}_L^T = (\sqrt{L}, 0,0, \dots, 0)^T$; substituting these intermediate results into (2.20) yields [7][8]

$$\Lambda = \frac{2\sqrt{S} \cdot \text{Re}\big[e^{-j\theta}\sqrt{L}\zeta_0\big] - SL}{N + \lambda_0 I} + \sum_{k=0}^{L-1}\left(\log\frac{1}{N + \lambda_k I} - \frac{|\zeta_k|^2}{N + \lambda_k I}\right), \tag{2.28}$$

where

$$\zeta_0 = \frac{1}{\sqrt{L}} \cdot \sum_{k=0}^{L-1} z_k. \tag{2.29}$$

From (2.28) the ML estimator can straightforwardly be obtained by computing the first derivative with respect to the estimation parameter q_i and equating it to zero. Doing this for the parameter vector $\mathbf{q}$ yields the following equations [7][8]:

$$t_1 = \frac{\partial \Lambda}{\partial \theta} = \frac{2\sqrt{S} \cdot \text{Im}\big[e^{-j\theta} \cdot \sqrt{L} \cdot \zeta_0\big]}{N + \lambda_0 \cdot I} = 0, \tag{2.30}$$

$$t_2 = \frac{\partial \Lambda}{\partial S} = \frac{\text{Re}\big[e^{-j\theta} \cdot \sqrt{L} \cdot \zeta_0\big] - \sqrt{S} \cdot L}{\sqrt{S} \cdot (N + \lambda_0 \cdot I)} = 0, \tag{2.31}$$

$$t_3 = \frac{\partial \Lambda}{\partial N} = -\frac{S \cdot L}{(N + \lambda_0 \cdot I)^2} + \sum_{k=0}^{L-1}\left(-\frac{1}{N + \lambda_k \cdot I} + \frac{|\zeta_k|^2}{(N + \lambda_k \cdot I)^2}\right) = 0, \tag{2.32}$$

$$t_4 = \frac{\partial \Lambda}{\partial I} = -\frac{\lambda_0 \cdot S \cdot L}{(N + \lambda_0 \cdot I)^2} + \sum_{k=0}^{L-1}\left(-\frac{\lambda_k}{N + \lambda_k \cdot I} + \frac{\lambda_k \cdot |\zeta_k|^2}{(N + \lambda_k \cdot I)^2}\right) = 0. \tag{2.33}$$

Further solving (2.30) and (2.31) delivers the respective estimators for the carrier phase and the signal power in closed form, i.e.

$$\hat{\theta} = \arg(\zeta_0) = \arg\left(\sum_{k=0}^{L-1} z_k\right) \tag{2.34}$$

and

$$\hat{S} = \frac{1}{L}\left(\text{Re}[e^{-j\hat{\theta}}\zeta_0]\right)^2 = \left|\frac{1}{L} \cdot \sum_{k=0}^{L-1} z_k\right|^2. \tag{2.35}$$

Unfortunately no closed form solution for (2.32) and (2.33) can be obtained, thus resorting to e.g. the Newton-Raphson algorithm (see Section 2.4.3) is required. However, solving (2.32) and (2.33) in this way is easier than in the case with residual frequency error (2.21)-(2.25). By close inspection of (2.32) and (2.33) it becomes clear that the spectral shape of the fading component represented by λ_k must be known *a priori* which is not realistic in practice.

2.4.2 Strictly Bandlimited Fading with Constant PSD

As mentioned before, the spectral shape of the interference component must be known to arrive at an ML estimator solution, which is also reflected in (2.32) and (2.33). According to [20] the power and bandwidth of the interference component are the predominant factors, whereas the spectral shape of the interference component is practically of little importance; this is also supported by simulation results published in [1]. Even though Butterworth and Jakes spectral shapes are considered for the time-selective fading in this work, above arguments motivate the development of an analytical framework resorting to a rectangular PSD for the interference component. The latter can be formulated as

$$\lambda_k = \begin{cases} \lambda_0, & k \in \mathcal{L}_0, L_0 = |\mathcal{L}_0| \\ 0, & k \in \mathcal{L}_1, L_1 = |\mathcal{L}_1| = L - L_0 \end{cases}, \tag{2.36}$$

where $\mathcal{L}_0$ represents a measure of the discrete bandwidth of the interference. However, substituting (2.36) into (2.32) and (2.33) after some algebra yields

$$t_3 = \frac{\partial \Lambda}{\partial N} = \frac{1}{N^2} + \sum_{k=\mathcal{L}_1} |\zeta_k|^2 - \frac{L - L_0}{N} = 0 \tag{2.37}$$

and

$$t_4 = \frac{\partial \Lambda}{\partial I} = -\frac{\lambda_0 \cdot S \cdot L}{(N + \lambda_0 I)^2} + \frac{\lambda_0}{(N + \lambda_0 I)^2} \sum_{k \in \mathcal{L}_0} |\zeta_k|^2 - \frac{\lambda_0 L_0}{N + \lambda_0 I} = 0. \tag{2.38}$$

Next solving (2.37) provides a closed form solution for the noise power estimate, i.e.

$$\widehat{N} = \frac{1}{L - L_0} \sum_{k=\mathcal{L}_1} |\zeta_k|^2, \tag{2.39}$$

which by close inspection corresponds to the part of the spectrum occupied by thermal noise only; indeed, this result approves the "heuristic" framework for noise power estimation established in [1] and [6] to be a ML solution under the given conditions.

Further solving (2.38) provides a closed form solution for the interference power estimate, i.e.,

$$\hat{I} = \frac{1}{\lambda_0 L_0} \sum_{k \in \mathcal{L}_0} |\zeta_k|^2 - \frac{\hat{S} \cdot L}{\lambda_0 L_0} - \frac{\widehat{N}}{\lambda_0}. \tag{2.40}$$

Recalling that the time-selective fading process η_k was normalized to unit variance, it is $\lambda_0 = L/L_0$ because $\frac{1}{L} \sum_{k=0}^{L-1} \lambda_k = \frac{1}{L} \lambda_0 L_0 = 1$. Plugging this into (2.40) yields

$$\hat{I} = \frac{1}{L} \sum_{k \in \mathcal{L}_0} |\zeta_k|^2 - \hat{S} - \frac{L_0 \widehat{N}}{L} = \frac{1}{L} \sum_{k=0}^{L-1} |\zeta_k|^2 - \hat{S} - \widehat{N}. \tag{2.41}$$

Finally, taking the second order moment of the receiver samples into account, i.e. $M_2 = \frac{1}{L}\sum_{k=0}^{L-1}|z_k|^2 = \frac{1}{L}\sum_{k=0}^{L-1}|\zeta_k|^2$, the interference power estimate can be stated as

$$\hat{I} = M_2 - \hat{S} - \widehat{N}, \tag{2.42}$$

which analogously to above approves the "heuristic" framework for interference power estimation established in [1] and [6] to be an ML solution.

2.4.3 The Newton-Raphson Method

Considering the above discussed estimation framework, it is clear that estimators based on the analysis presented in Section 2.4.1 have to solve nonlinear cost functions. Nonetheless, several methods exist for finding a zero of a nonlinear function, i.e. $f(u) = 0$: the bisection method, the rule of false position, the secant method the Newton-Raphson method, and the method of Bus and Dekkar are amongst others mentioned in the literature for that purpose. Important figures of merit of such methods for practical implementations are the demand to provide an initial interval, the guarantee to converge into a valid solution and the convergence rate, i.e. the speed of convergence. For the above-mentioned methods, Table 1 provides a comparison of those key properties [28, pp. 35-58]:

Method	Initial interval required?	Guaranteed to find a zero?	Rate of Convergence
Bisection	Yes	Yes	1
False position	Yes	Yes	$1 - 1.62$
Secant	No	No	1.62
Bus and Dekker	Yes	Yes	$1 - 1.62$
Newton-Raphson	No	Yes (requires good initial estimate)	2

Table 1: Comparison of properties of methods to solve nonlinear equations

From the table above it is easy to understand that the Newton-Raphson algorithm provides some advantages, i.e. it does not require an initial interval and it converges relatively fast, whilst it still requires a good initialization. For the latter, the simulation re-

sults presented in this thesis generally use (2.39) and (2.42) as the initial guess. However, from Section 2.4.1 it is known that two nonlinear equations, i.e. (2.32) and (2.33) have to be solved simultaneously. Thus, the nonlinear problem to be solved resorts to

$$\mathbf{f}(\mathbf{u}) = 0, \tag{2.43}$$

where for the given case $\mathbf{f} = \{t_3, t_4\}^T$ denotes the vector of the nonlinear equations – (2.32) and (2.33) – and the parameter vector $\mathbf{u} = \{N, I\}^T$. It is evident that this two-dimensional case is more difficult to tackle than one dimensional problems. Although there are no good general methods available for systems consisting of more than one nonlinear equation, literature typically suggests the Newton-Raphson method whilst keeping in mind its susceptibility to initialization [25, pp. 347-393].

In the neighbourhood of $\mathbf{u}$ each of the functions in $\mathbf{f}$, being denoted f_i, can be approximated by Taylor series such that

$$f_i(\mathbf{u} + \delta\mathbf{u}) = f_i(\mathbf{u}) + \sum_{j=1}^{N} \frac{\partial f_i(\mathbf{u})}{\partial u_j} \delta u_j + G(\delta\mathbf{u}^2), \tag{2.44}$$

with $N = 2$ for the given case; the summation term can be rewritten by the Jacobian matrix $\mathbf{J}$, i.e. [25, pp. 347-393]

$$J_{ij} = \frac{\partial f_i(\mathbf{u})}{\partial u_j}, \tag{2.45}$$

which decomposes into

$$\mathbf{J} = \begin{bmatrix} J_{11} & J_{12} \\ J_{21} & J_{22} \end{bmatrix} = \begin{bmatrix} \dfrac{\partial t_3}{\partial N} & \dfrac{\partial t_3}{\partial I} \\ \dfrac{\partial t_4}{\partial N} & \dfrac{\partial t_4}{\partial I} \end{bmatrix}; \tag{2.46}$$

by using (2.32) and (2.33) this further resolves to:

$$J_{11} = \frac{\partial t_3}{\partial N} = \frac{2 \cdot S \cdot L}{(N + \lambda_0 \cdot I)^3} + \sum_{k=0}^{L-1} \left(\frac{1}{(N + \lambda_k \cdot I)^2} - \frac{2 \cdot |\zeta_k|^2}{(N + \lambda_k \cdot I)^3} \right), \tag{2.47}$$

$$J_{12} = \frac{\partial t_3}{\partial I} = \frac{2 \cdot S \cdot L \cdot \lambda_0}{(N + \lambda_0 \cdot I)^3} + \sum_{k=0}^{L-1} \left(\frac{\lambda_k}{(N + \lambda_k \cdot I)^2} - \frac{2 \cdot \lambda_k \cdot |\zeta_k|^2}{(N + \lambda_k \cdot I)^3} \right), \tag{2.48}$$

$$J_{21} = \frac{\partial t_4}{\partial N} = \frac{2 \cdot S \cdot L \cdot \lambda_0}{(N + \lambda_0 \cdot I)^3} + \sum_{k=0}^{L-1} \left(\frac{\lambda_k}{(N + \lambda_k \cdot I)^2} - \frac{2 \cdot \lambda_k \cdot |\zeta_k|^2}{(N + \lambda_k \cdot I)^3} \right), \tag{2.49}$$

$$J_{22} = \frac{\partial t_4}{\partial I} = \frac{2 \cdot S \cdot L \cdot \lambda_0^2}{(N + \lambda_0 \cdot I)^3} + \sum_{k=0}^{L-1} \left(\frac{\lambda_k^2}{(N + \lambda_k \cdot I)^2} - \frac{2 \cdot \lambda_k^2 \cdot |\zeta_k|^2}{(N + \lambda_k \cdot I)^3} \right). \tag{2.50}$$

However, plugging (2.45) into (2.44) yields

$$f_i(\mathbf{u} + \delta\mathbf{u}) = f_i(\mathbf{u}) + \mathbf{J} \cdot \delta\mathbf{u} + G(\delta\mathbf{u}^2). \tag{2.51}$$

From there a set of linear equations which move each nonlinear function closer to zero can be obtained by neglecting higher order terms, i.e. $G(\delta\mathbf{u}^2)$, and by setting $f_i(\mathbf{u} + \delta\mathbf{u}) = 0$. By solving for the parameter correction vector this becomes

$$\delta\mathbf{u} = -\mathbf{J}^{-1} \cdot f_i(\mathbf{u}). \tag{2.52}$$

It is to be noticed that the computation of the inverse of $\mathbf{J}$ can lead to singularity issues, thus literature suggests to apply Lower-Upper decomposition, i.e. $\mathbf{J} = \mathbf{L} \cdot \mathbf{U} \rightarrow \mathbf{J}^{-1} = \mathbf{U}^{-1} \cdot \mathbf{L}^{-1}$, where $\mathbf{L}$ und $\mathbf{U}$ are lower and upper triangular matrices, respectively. Alternatively, QR decomposition is suggested tackling the issues according to $\mathbf{J} = \mathbf{Q} \cdot \mathbf{R} \rightarrow \mathbf{J}^{-1} = \mathbf{R}^{-1} \cdot \mathbf{Q}^{-1}$, where $\mathbf{Q}$ is an orthogonal matrix and $\mathbf{R}$ is an upper triangular matrix. Literature attests QR decomposition a better performance compared to LU decomposition [25, pp. 347-393][29, pp. 80-89]. However, during simulations it was observed that the pure inverse of $\mathbf{J}$ and the inverse through QR decomposition for some cases exhibit issues with singularities in the matrices.

The solution of the parameter vector fulfilling (2.43) can iteratively be found under the premises of an appropriately chosen initialization value using

$$\mathbf{u}_{n+1} = \mathbf{u}_n + \delta\mathbf{u}, \tag{2.53}$$

where the index n indicates the n-th iteration [25, pp. 347-393].

Applying the above stated to the investigated case yields

$$\delta\begin{bmatrix} N \\ I \end{bmatrix} = -\begin{bmatrix} \dfrac{\partial t_3}{\partial N} & \dfrac{\partial t_3}{\partial I} \\ \dfrac{\partial t_4}{\partial N} & \dfrac{\partial t_4}{\partial I} \end{bmatrix}^{-1} \cdot \begin{bmatrix} t_3 \\ t_4 \end{bmatrix}. \tag{2.54}$$

For the sake of completeness, the iteration step followed from (2.53) is trivially achieved by

$$\begin{bmatrix} N \\ I \end{bmatrix}_{n+1} = \begin{bmatrix} N \\ I \end{bmatrix}_n + \delta\begin{bmatrix} N \\ I \end{bmatrix}. \tag{2.55}$$

2.5 Theoretical Performance Limits

To assess the performance of the considered parameter estimation framework benchmarking is required, which for parameter estimations is typically done by comparison with so called *Cramer-Rao lower bounds* (CRLBs) or *modified Cramer-Rao lower bounds* (MCRLBs) providing fundamental theoretical limits to the variance of any unbiased estimator [9, pp. 53-55]. Lower bounds are important in the realm of parameter estimation, however, it is refrained from overextending this vast topic in the context of this thesis; nevertheless, the necessary bounds are stated and explained briefly in Subsections 2.5.1 and 2.5.2 under relevant boundary conditions. Their asymptotic behaviour in terms of noise and interference is illuminated in Subsection 2.5.3.

2.5.1 Lower Bounds for Large Observation Lengths

This section provides the CRLBs for fading channels presuming large observation lengths, i.e. $L \gg L_\mu = 1/B_\mu T$, according to the original work in [7] based on the derivations presented in [20]; it is refrained from stating derivations, so that only the final re-

sults achieved in the original work are provided. It is to be noticed that Subsections 2.5.1.1-2.5.1.3 are based on [7], thus only additional sources are explicitly quoted therein.

2.5.1.1 CRLBs for Carrier Frequency and Phase

Synchronization is indispensable for efficient data transmission, thus the carrier frequency and phase offset have to be corrected requiring estimations. The latter are limited in their performance for the given channel for the carrier phase by

$$CRLB(\theta) = \frac{1 + K_R + \rho \cdot \left(1 + \frac{1}{K_R}\right) \cdot S_\mu(0)}{2\rho \cdot (1 + K_R) \cdot L} \tag{2.56}$$

and for the carrier frequency by

$$CRLB(\nu) = \frac{3 \cdot \left[1 + K_R + \rho \cdot \left(1 + \frac{1}{K_R}\right) \cdot S_\mu(0)\right]}{2\pi^2 \cdot \rho \cdot (1 + K_R) \cdot L^3}. \tag{2.57}$$

By close inspection of (2.56) and (2.57) it can be seen that the CRLBs only depend on the interference component related to the signal component in the spectrum, i.e. $S_\mu(0)$, rather than on the actual spectral shape of the interference.

2.5.1.2 CRLBs for Amplitude and Power Parameters

After synchronization the amplitude and power parameters can be estimated. By applying

$$J_{33} = \frac{2}{N} \cdot \frac{(1 + K_R) \cdot L}{1 + K_R + \rho \cdot \left(1 + \frac{1}{K_R}\right) \cdot S_\mu(0)}, \tag{2.58}$$

$$J_{44} = \frac{1}{N^2} \cdot \sum_{k=0}^{L-1} \left(\frac{1 + K_R}{1 + K_R + \rho \cdot \left(1 + \frac{1}{K_R}\right) \cdot S_\mu\left(\frac{k}{LT}\right)}\right)^2, \tag{2.59}$$

$$J_{45} = \frac{1}{NI} \cdot \sum_{k=0}^{L-1} \frac{\rho \cdot (1 + K_R)^2 \cdot S_\mu\left(\frac{k}{LT}\right)}{K_R \cdot \left[1 + K_R + \rho \cdot \left(1 + \frac{1}{K_R}\right) \cdot S_\mu\left(\frac{k}{LT}\right)\right]^2}, \tag{2.60}$$

$$J_{55} = \frac{1}{I^2} \cdot \sum_{k=0}^{L-1} \left(\frac{\rho \cdot \left(1 + \frac{1}{K_R}\right) \cdot S_\mu\left(\frac{k}{LT}\right)}{1 + K_R + \rho \cdot \left(1 + \frac{1}{K_R}\right) \cdot S_\mu\left(\frac{k}{LT}\right)} \right)^2, \tag{2.61}$$

the CRLBs for the amplitude a, the signal power, the noise and interference power can be stated as

$$CRLB(a) = \frac{1}{J_{33}}, \tag{2.62}$$

$$CRLB(S) = \frac{4a^2}{J_{33}}, \tag{2.63}$$

$$CRLB(N) = \frac{J_{55}}{J_{44} \cdot J_{55} - J_{45}^2}, \tag{2.64}$$

$$CRLB(I) = \frac{J_{44}}{J_{44} \cdot J_{55} - J_{45}^2}, \tag{2.65}$$

where (2.63) – (2.65) depend on the actual spectral shape of the interference component.

2.5.1.3   CRLBs for Power Ratios

Eventually the CRLBs for both power ratios the SNR and the SIR (or K_R) can be stated using (2.58) – (2.61) as

$$CRLB(\rho) = \frac{4a^2}{N^2} \cdot \frac{1}{J_{33}} + \frac{a^4}{N^4} \cdot \frac{J_{55}}{J_{44} \cdot J_{55} - J_{45}^2}, \tag{2.66}$$

$$CRLB(K_R) = \frac{4a^2}{I^2} \cdot \frac{1}{J_{33}} + \frac{a^4}{I^4} \cdot \frac{J_{44}}{J_{44} \cdot J_{55} - J_{45}^2}. \tag{2.67}$$

Akin to above, (2.66) and (2.67) depend on the spectral shape of the interference component.

2.5.2 Lower Bounds for Strictly Bandlimited and Flat Doppler Spectra

This section provides the CRLBs for fading channels presuming large observation lengths, i.e. $L \gg L_\mu = 1/B_\mu T$, as well as strictly band-limited and frequency-flat Doppler spectrum, i.e.

$$S_\mu(f) = \begin{cases} \dfrac{1}{B_\mu T}, & |f| \leq f_\mu \\ 0, & |f| > f_\mu \end{cases}. \tag{2.68}$$

The presented elaborations are based on the analysis in [7]; it is refrained from presenting derivations, only the final results achieved in the original work are provided. It is to be noticed that Subsections 2.5.2.1 - 2.5.2.2 are based on [7], thus only additional sources are explicitly quoted therein.

Recalling (2.56), (2.57), (2.62) and (2.63) it is clear that they do not change for the underlying limitations.

2.5.2.1 CRLBs for Power Parameters

As already mentioned, (2.68) does not influence (2.63); however, it is more convenient to use the *normalized CRLB* (NCRLB) which for the signal power resorts to

$$NCRLB(S) = \frac{CRLB(S)}{S^2} = \frac{2 \cdot \left[1 + K_R + \rho \cdot \left(1 + \frac{1}{K_R}\right) \cdot S_\mu(0)\right]}{\rho \cdot (1 + K_R) \cdot L}. \tag{2.69}$$

Using the condition in (2.68), the equations (2.59) – (2.61) can be simplified to

$$J_{44} = \frac{L}{N^2} \cdot \left\{ (1 - B_\mu T) + B_\mu T \cdot \left(\frac{1 + K_R}{1 + K_R + \rho \cdot \left(1 + \frac{1}{K_R}\right) \cdot S_\mu(0)} \right)^2 \right\} \tag{2.70}$$

$$= \frac{\chi_{44} \cdot L B_\mu T}{N^2},$$

$$J_{45} = \frac{L B_\mu T}{NI} \cdot \frac{\rho \cdot (1 + K_R)^2 \cdot S_\mu(0)}{K_R \cdot \left[1 + K_R + \rho \cdot \left(1 + \frac{1}{K_R}\right) \cdot S_\mu(0)\right]^2} = \frac{\chi_{45} \cdot L B_\mu T}{NI}, \tag{2.71}$$

$$J_{55} = \frac{LB_\mu T}{I^2} \cdot \left(\frac{\rho \cdot \left(1 + \frac{1}{K_R}\right) \cdot S_\mu(0)}{1 + K_R + \rho \cdot \left(1 + \frac{1}{K_R}\right) \cdot S_\mu(0)} \right)^2 = \frac{\chi_{55} \cdot LB_\mu T}{I^2}, \qquad (2.72)$$

where χ_{44}, χ_{45}, and χ_{55} yield

$$\chi_{44} = \left\{ \left((B_\mu T)^{-1} - 1\right) + \left(\frac{1 + K_R}{1 + K_R + \rho \cdot \left(1 + \frac{1}{K_R}\right) \cdot S_\mu(0)} \right)^2 \right\} \qquad (2.73)$$

$$\chi_{45} = \frac{\rho \cdot (1 + K_R)^2 \cdot S_\mu(0)}{K_R \cdot \left[1 + K_R + \rho \cdot \left(1 + \frac{1}{K_R}\right) \cdot S_\mu(0)\right]^2}, \qquad (2.74)$$

$$\chi_{55} = \left(\frac{\rho \cdot \left(1 + \frac{1}{K_R}\right) \cdot S_\mu(0)}{1 + K_R + \rho \cdot \left(1 + \frac{1}{K_R}\right) \cdot S_\mu(0)} \right)^2. \qquad (2.75)$$

With that the CRLBs for noise and interference power can be rewritten in normalized form as

$$NCRLB(N) = \frac{CRLB(N)}{N^2} = \frac{1}{LB_\mu T} \cdot \frac{\chi_{55}}{\chi_{44} \cdot \chi_{45} - \chi_{45}^2} \qquad (2.76)$$

and

$$NCRLB(I) = \frac{CRLB(I)}{I^2} = \frac{1}{LB_\mu T} \cdot \frac{\chi_{44}}{\chi_{44} \cdot \chi_{45} - \chi_{45}^2}. \qquad (2.77)$$

2.5.2.2 CRLBs for Power Ratios

Defining

$$J_{33} = \frac{2L \cdot \chi_{33}}{N}; \qquad (2.78)$$

the parameter χ_{33} can be retained from (2.58) as

$$\chi_{33} = \frac{1 + K_R}{1 + K_R + \rho \cdot \left(1 + \frac{1}{K_R}\right) \cdot S_\mu(0)}.$$
(2.79)

With that the NCRLBs for SNR and SIR resume for the band-limited and flat-fading case to

$$NCRLB(\rho) = \frac{CRLB(\rho)}{\rho^2} = \frac{2}{\chi_{33} \cdot \rho \cdot L} + \frac{1}{LB_\mu T} \cdot \frac{\chi_{55}}{\chi_{44} \cdot \chi_{45} - \chi_{45}^2}$$
(2.80)

and

$$\begin{aligned} NCRLB(K_R) &= \frac{CRLB(K_R)}{K_R^2} \\ &= \frac{2}{\chi_{33} \cdot \rho \cdot L} + \frac{1}{LB_\mu T} \cdot \frac{\chi_{44}}{\chi_{44} \cdot \chi_{45} - \chi_{45}^2}, \end{aligned}$$
(2.81)

respectively.

2.5.3 Jitter Floor Behaviour

Recalling the signal model, it is clear that two nuisance components, i.e. noise and interference, limit the achievable estimation performance. Subsequent sections investigate the impact of one nuisance parameter vanishing whilst the other remaining constant on the (N)CRLBs as introduced before.

2.5.3.1 Vanishing Noise Component

Having the noise component vanishing, i.e. $\rho \to \infty$, results in a jitter floor reflecting the constant interference power for the (N)CRLBs provided for the carrier parameters in (2.56) and (2.57), for the power parameters in (2.69), (2.76) and (2.77), as well as for the power ratios in (2.80) and (2.81):

$$CRLB(\theta)|_{\rho\to\infty} = \frac{S_\mu(0)}{2 \cdot K_R L}, \tag{2.82}$$

$$CRLB(v)|_{\rho\to\infty} = \frac{3 \cdot S_\mu(0)}{2\pi^2 \cdot K_R L^3}, \tag{2.83}$$

$$NCRLB(S)|_{\rho\to\infty} = \frac{2 \cdot S_\mu(0)}{K_R L}, \tag{2.84}$$

$$NCRLB(N)|_{\rho\to\infty} = \frac{1}{L \cdot (1 - B_\mu T)}, \tag{2.85}$$

$$NCRLB(I)|_{\rho\to\infty} = \frac{1}{L B_\mu T}, \tag{2.86}$$

$$NCRLB(\rho)|_{\rho\to\infty} = \frac{2 \cdot S_\mu(0)}{K_R L} + \frac{1}{L \cdot (1 - B_\mu T)}, \tag{2.87}$$

$$NCRLB(K_R)|_{\rho\to\infty} = \frac{2 \cdot S_\mu(0)}{K_R L} + \frac{1}{L B_\mu T}. \tag{2.88}$$

2.5.3.2 Vanishing Interference Component

Having the interference component vanishing, i.e. $K_R \to \infty$, results in AWGN conditions; hence, it is

$$CRLB(\theta)|_{K_R\to\infty} = \frac{1}{2 \cdot \rho \cdot L}, \tag{2.89}$$

$$CRLB(v)|_{K_R\to\infty} = \frac{3}{2\pi^2 \cdot L \cdot (L^2 - 1) \cdot \rho}, \tag{2.90}$$

$$NCRLB(S)|_{K_R\to\infty} = \frac{2}{\rho \cdot L}, \tag{2.91}$$

$$NCRLB(N)|_{K_R\to\infty} = \frac{1}{L}, \tag{2.92}$$

$$NCRLB(\rho)|_{K_R\to\infty} = \frac{1}{L} \cdot \left(1 + \frac{2}{\rho}\right). \tag{2.93}$$

By close inspection it is clear that the results stated above match with (N)CRLBs for DA parameter estimations published for AWGN conditions in the open literature.

2.6   Simulations

This subchapter examines the simulation framework used to evaluate the analytical results from above. For the latter the focus clearly was on the estimation framework discussed in the Subchapters 2.4.1 and 2.4.2. Therefore, after introducing the standard simulation settings in Subsection 2.6.1, which is the considered baseline for subsequently presented results, Section 2.6.2 discusses the carrier recovery performance and Sections 2.6.3 and 2.6.4 show the estimation performance of the power parameters and power ratios, respectively.

2.6.1 Standard Simulation Settings

If not otherwise stated, the following simulation settings, subsequently denoted as *standard settings* and tailored to the precursor work in [1] and [2], apply:

- Channel settings:
  - Time-selective and frequency-flat Rician fading channel
  - Scatter component is implemented either
    - isotropic by a Jakes filter, indicated as $RICE_J$ (implemented as 201 tapped FIR filter structure) or
    - non-isotropic by a 10th order Butterworth filter indicated as $RICE_{BW}$.
  - The cut-off frequency of the LPF equals to f_μ.
  - Normalized Doppler spread: $B_\mu T_S = 0.05$.
  - Angle of Arrival (AoA): $\alpha = 90°$.
- Carrier settings:
  - Phase error: $\theta \in [-\pi, \pi)$.
  - Frequency error: $\nu = \Delta f T \in [-0.1, 0.1]$.
- Estimation settings:
  - Ideal symbol timing.
  - QPSK training sequence with $L = 1024$ symbols.
  - Ideal estimation of the Doppler spread and AoA (Genie).
  - Guard band of 30 DFT bins to mitigate effects introduced by the channel LPF.
  - Stopping criterion for Newton-Raphson method: $10^{-12} \geq |\delta N| + |\delta I|$
  - Power parameter and power ratio estimation is done either
    - by applying the framework detailed in Section 2.4.1, which requires a non-linear estimation procedure, hence results are indexed with the abbreviation NL (*non-linear*) or

- ▪ by applying the simplified framework according to Section 2.4.2, which according to its origin as a heuristic method (presented in [6]) is denoted as HE (*heuristic estimation*).
  - o The NL method is initialized with the HE method.

2.6.2 Carrier Recovery

The performance of carrier parameter recovery was investigated in due detail in [1], this section extends the work presented therein and also investigates the performance in dependence of the AoA. In the context of this thesis the frequency estimator proposed by Rife and Boostyn in [23] is used, an unbiased and well proven method capable to perform close to the theoretical limit. Moreover the simulation results are benchmarked with the (N)CRLBs provided in (2.56) and (2.57) applied to the true LPF shape of the scatter components.

Figures 2.9 and 2.10 depict the carrier frequency and phase estimation performance in terms of the (*normalized*) *mean square error* ((N)MSE) over SNR, respectively, at a fixed Doppler spread of $B_\mu T_S = 0.1$. Different levels of interference represented by different K_R values are distinguished in colour (black, blue and green); an AWGN case (red) is indicated as well, this way highlighting the deterioration effect of the interference. Both isotropic and non-isotropic numerical results are included; all are benchmarked by their associated (N)CRLB. Again, the match of numerical results with their associated (N)CRLBs can be observed. Nonetheless, in Figure 2.9 a deviation of the performance of the Rife-Boorstyn estimator from the CRLB for AWGN [9] at high SNR can be observed, a phenomenon well known which originates form the estimator algorithmic: the additional frequency jitter visible in the higher SNR regime originates from the DFT performed, which of course has got finite spectral resolution. The actual frequency estimate is established from the periodogram in combination with interpolation introducing extra jitter; the latter, however, can be reduced by increasing the spectral resolution of the DFT to the expense of a higher computational load.
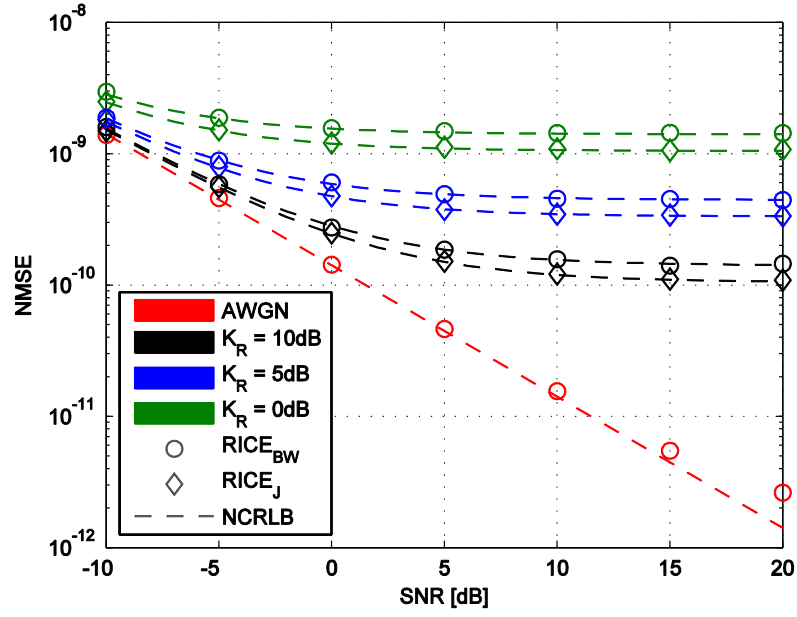
Figure 2.9: NMSE of the carrier frequency
estimates over SNR ($B_\mu T_S = 0.1$)
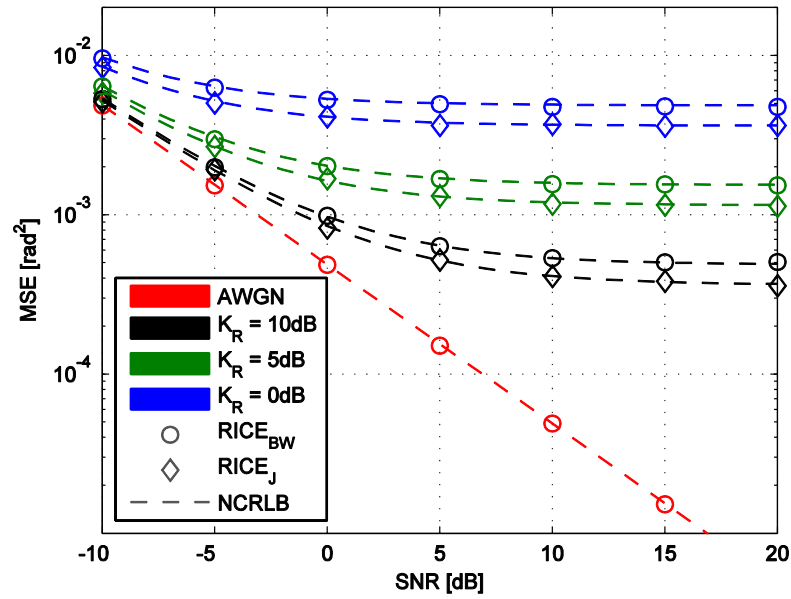
Figure 2.10: MSE of the carrier phase
estimates over SNR ($B_\mu T_S = 0.1$)

The Figures 2.11 - 2.14 depict the performance of carrier parameter (normalized frequency and phase) estimation for isotropic and non-isotropic scattering at different levels of Doppler spread presuming both fixed $SNR = 10\ dB$ and $K_R = 10\ dB$. The remaining simulation settings follow the standard settings.
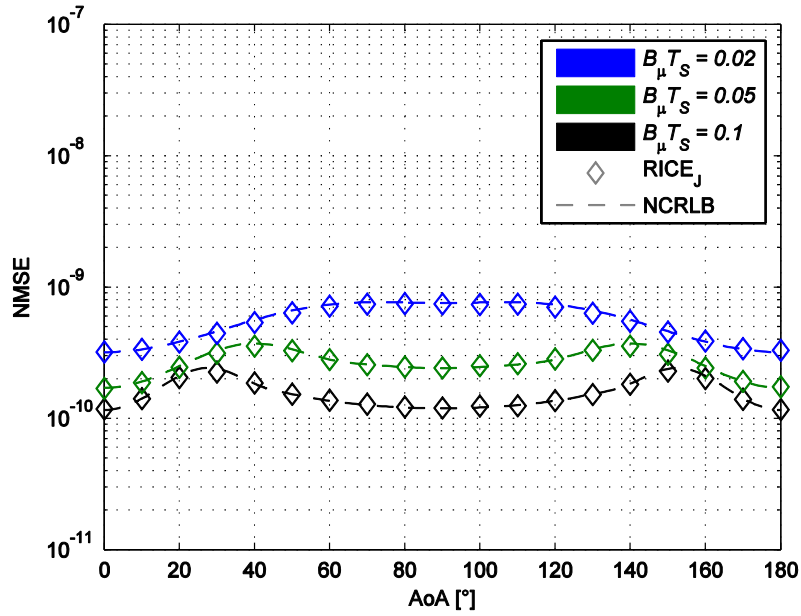
Figure 2.11: Carrier frequency recovery performance vs. AoA for isotropic scattering ($SNR = 10\ dB$, $K_R = 10\ dB$)
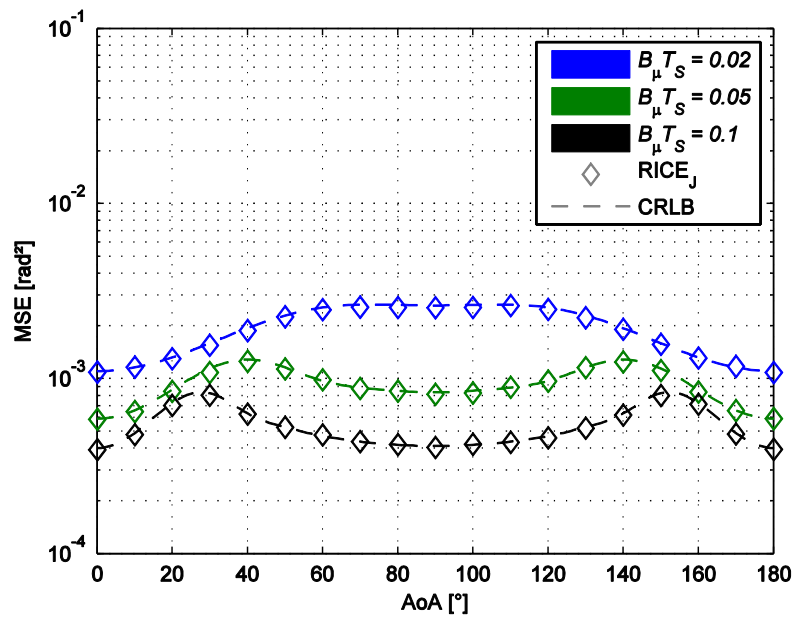
Figure 2.12: Carrier phase recovery performance vs. AoA for isotropic scattering ($SNR = 10\ dB$, $K_R = 10\ dB$)
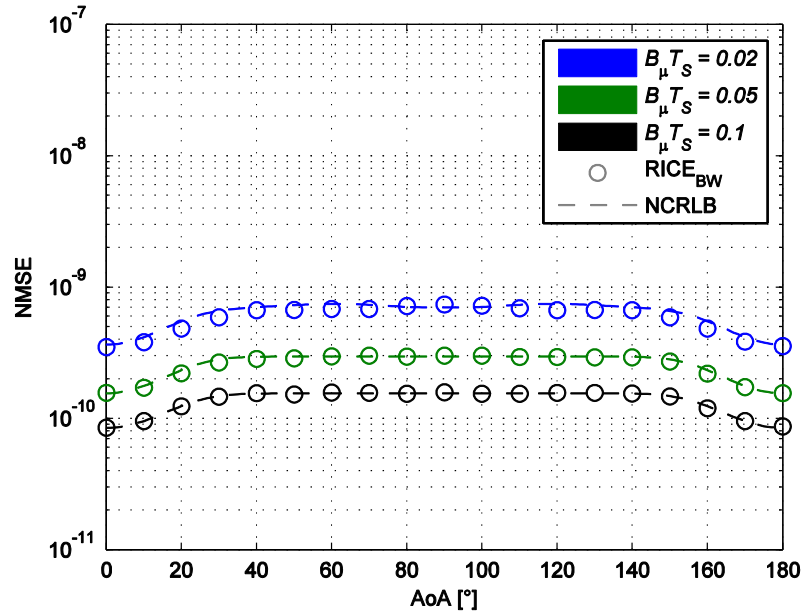
Figure 2.13: Carrier frequency recovery performance vs. AoA for non-isotropic scattering ($SNR = 10\ dB, K_R = 10\ dB$)
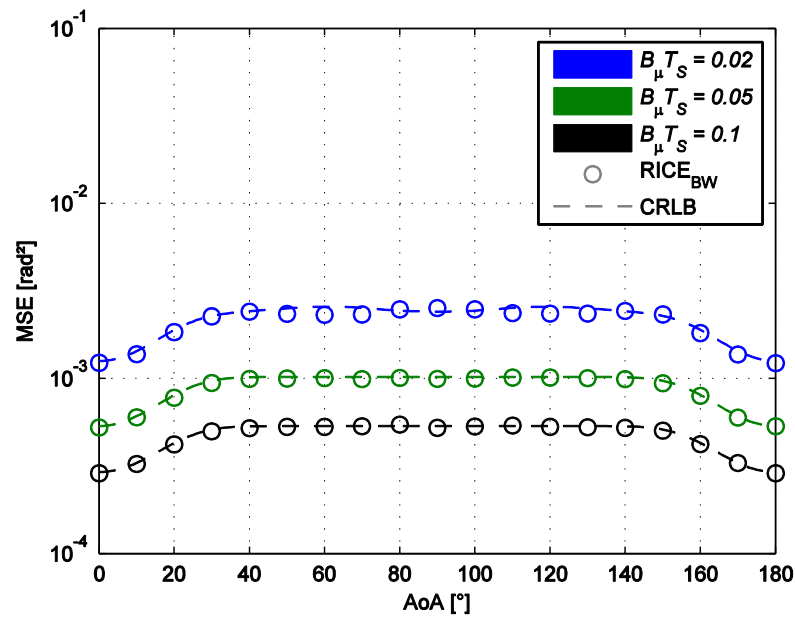
Figure 2.14: Carrier phase recovery performance vs. AoA for non-isotropic scattering ($SNR = 10\ dB, K_R = 10\ dB$)

In Figures 2.11 - 2.14 it can be observed that the numerical results match with the (N)CRLBs, thus the estimator may be regarded as optimal for the investigated case; an observation which is also supported by the results provided in [1, pp. 112-115] for a fixed AoA of 90° with variable SNR at different K_R. However, having observed the match between numerical results and the analytical (N)CRLBs, it can be concluded that the achievable performance depends on the ratio of the signal component and the spec-

tral interference component which are located at the zero frequency bin in the discrete spectrum after frequency correction. In other words, the achievable performance is bound to the ratio of the signal component and the spectrally related scatter component.

2.6.3 Power Parameter Estimation

After having corrected the carrier offsets, i.e. frequency and phase, the power parameters can be tackled. Within the following subsections the estimation performance in terms of accuracy for the power parameters, i.e. the signal power S, the noise power N and the interference power I, is investigated, benchmarked and discussed. It is to be noticed that two basic methods are compared – the one described in Section 2.4.1 which in the sequel is loosely denoted as NL method because of its nonlinear algorithmic and the one introduced in Section 2.4.2 which is loosely denoted as *heuristic estimation* (HE) which corresponds to the original work presented in [6]. The evidence for the latter to be a ML solution under strictly band-limited and flat fading conditions was found in [7] already.

2.6.3.1   Signal Power Estimation

From Section 2.4 it is known that both NL and HE method use the same framework for signal power estimations, hence subsequent performance curves are valid for both. Figure 2.15 depicts the jitter performance in terms the NMSE over SNR. Simulation results for isotropic (diamonds) and non-isotropic (circlets) scattering for different severances – indicated by $K_R = \{0, 5, 10\}dB$ – are visualized. NCRLBs are indicated for the results as dashed and appropriately coloured lines; an additional NCRLB plotted as red dashed line indicates the AWGN case. The standard settings apply. From Figure 2.15 it can clearly be seen that the lower bounds introduced in Section 2.5 again provide a good match with the simulation results.

Figure 2.16 investigates the *normalized mean estimator error* (NMEV) for signal power estimations. Standard settings apply, but different K_R values are used. The red dashed line indicates the *normalized true value* (NTV). Simulation results for isotropic (diamonds) and non-isotropic (circlets) scattering are indicated connected by appropriately coloured dotted lines to improve the readability. Nonetheless, any deviation from the NTV represents a bias. It can clearly be seen that towards the higher SNR regime a little bias remains which depends on K_R and on the scatter model used.
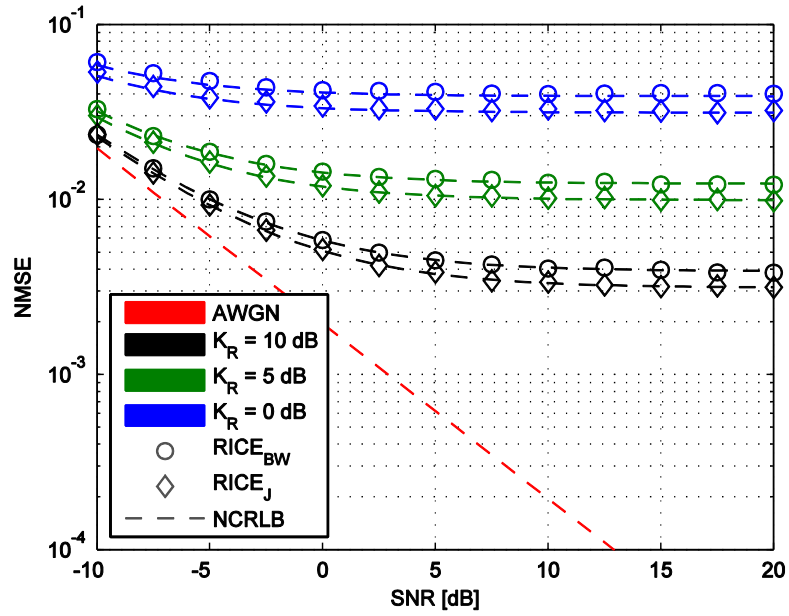
Figure 2.15: NMSE for signal power estimation
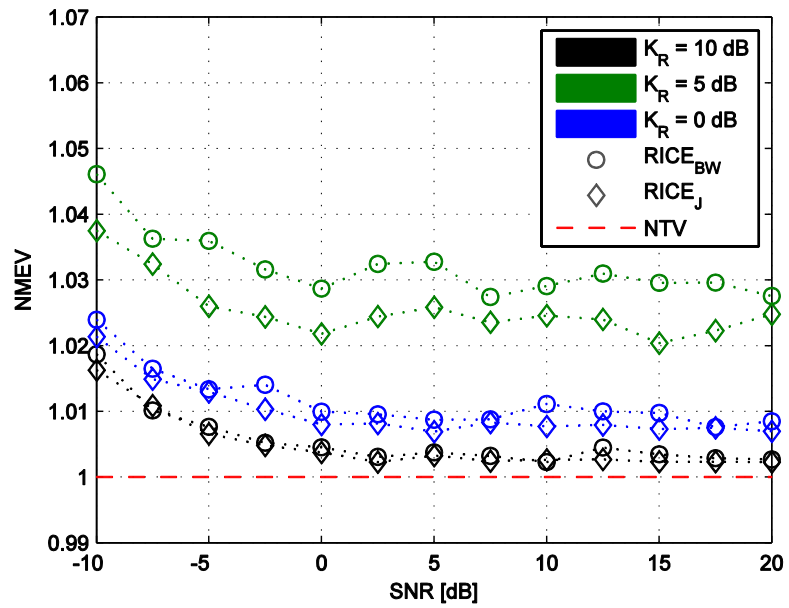
Figure 2.16: NMEV for signal power estimation

Figures 2.17 and 2.18 depict the signal power estimation performance in terms of the NMSE at variable AoA for both methods, NL and HE, because the signal power is estimated in the same way for both methods. However, the colour-coding is given in the plotted legends, standard settings apply; appropriate NCRLBs are indicated as well. It can be observed that the estimation performance reaches the predicted NCRLB.
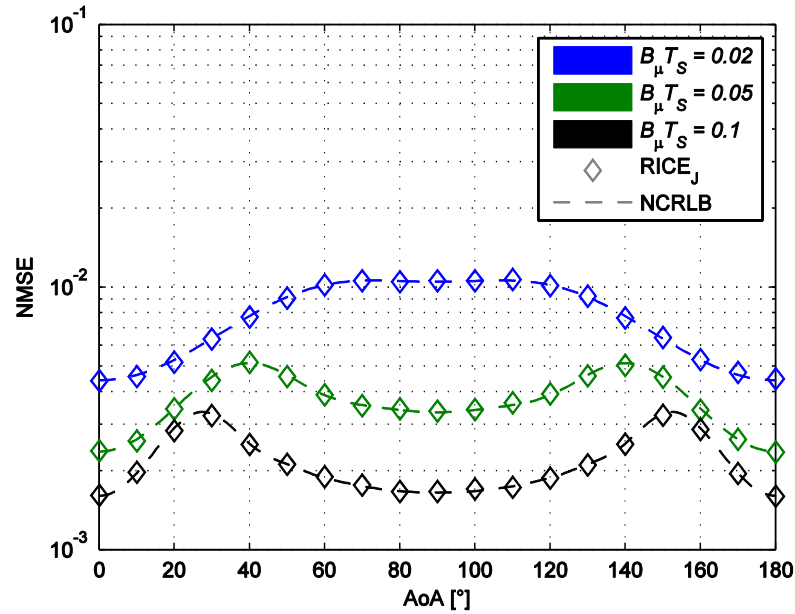
Figure 2.17: Signal power estimation performance vs. AoA for
isotropic scattering ($SNR = 10\ dB, K_R = 10\ dB$)
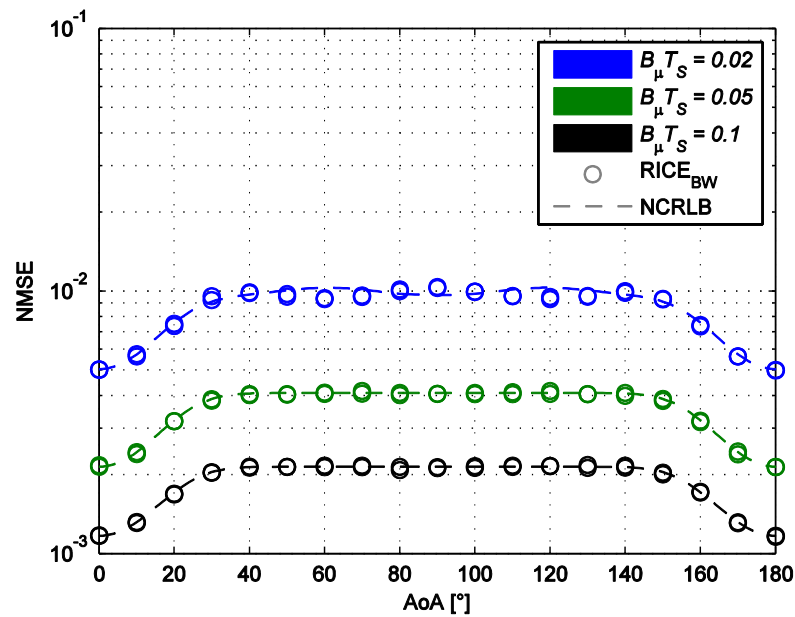
Figure 2.18: Signal power estimation performance vs. AoA for
non-isotropic scattering ($SNR = 10\ dB, K_R = 10\ dB$)

2.6.3.2 Noise Power Estimation

Figures 2.19 and 2.20 investigate the jitter behaviour of the noise estimates over SNR;
the former depicts the NMSE and the latter the *mean estimator value* (MEV) for iso-
tropic scattering in a) and for non-isotropic scattering in b) at $K_R = \{0, 5, 10\}dB$. Both
figures depict results for the NL (circlets/diamonds with transparent body) and the HE

(circlets/diamonds with coloured body) estimation method according to the applicable standard settings. Both figures use the same colour-coding, but in Figure 2.20 the legend was removed; additionally the true value is plotted in Figure 2.20 as red dashed line. However, it can clearly be seen that a little bias effect (deviation from the true value in Figure 2.20) in the medium to higher SNR regime causes a significant deviation from the NCRLB; not surprisingly this effect is more severe for small K_R values; also by applying the NL estimation framework the estimation error remains higher than with the HE method, although the latter is analytically limited to strictly band limited and flat fading.

Figure 2.21 indicates the noise power estimation performance with respect to the AoA; results for isotropic scattering are depicted in a) and for non-isotropic scattering in b) applying both NL (circlets/diamonds with transparent body) and HE (circlets/diamonds with coloured body) estimators. Different Doppler spreads, i.e. $B_\mu T_S = \{0.02, 0.05, 0.1\}$, are indicated in blue, green and black respectively. The NCRLBs are plotted as appropriately colour-coded dashed lines. It can be observed that the simulation results do not achieve the NCRLB, because of the adherent bias. However, the AoA does obviously not influence the performance. Both estimation methods exhibit a similar performance with noise power estimates.
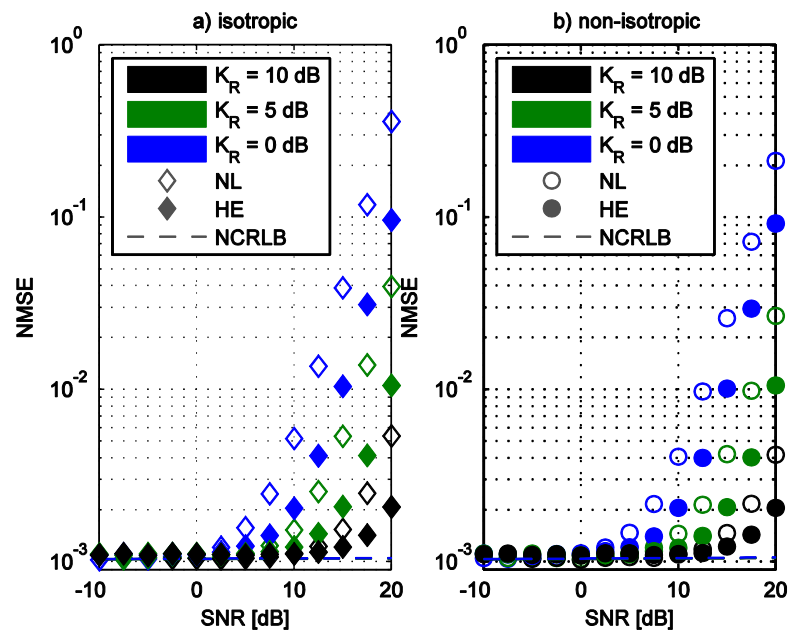
Figure 2.19: NMSE of the noise power estimates for
isotropic and non-isotropic scattering
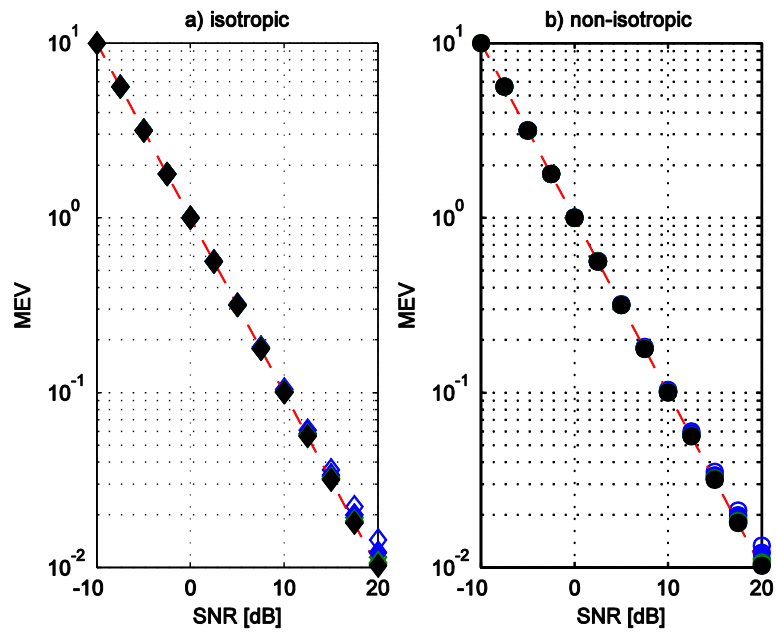
Figure 2.20: MEV of the noise power estimates for
isotropic and non-isotropic scattering
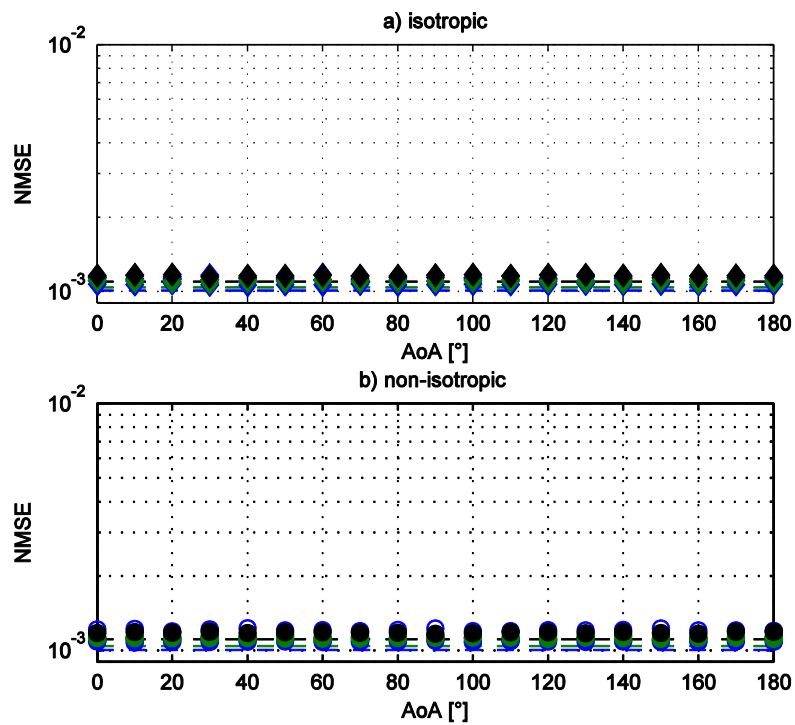
Figure 2.21: Noise power estimation performance vs. AoA
$(SNR = 10\ dB, K_R = 10\ dB)$

2.6.3.3 Interference Power Estimation

Figures 2.22 and 2.23 investigate the jitter behaviour of the interference power estimates over SNR; the former depicts the NMSE and the latter the NMEV for isotropic scattering in a) and for non-isotropic scattering in b) at $K_R = \{0, 5, 10\}dB$ colour-coded in blue, green and black, respectively. Both figures depict results for the NL (circlets/diamonds with transparent body) and the HE (circlets/diamonds with coloured body) estimation method according to the applicable standard settings. The associated NCRLBs are appropriately colour-coded and indicated as dashed lines in Figure 2.22. The NTV is printed as red dashed line in Figure 2.23 from which it can clearly be seen that bias effects occur. The bias explains the little deviation from the NCRLB in Figure 2.22. Moreover, the NL estimates increasingly deviate from their associated NCRLB with higher SNR due to the increasing bias.

Figure 2.24 indicates the interference power estimation performance with respect to the AoA; results for isotropic scattering are depicted in a) and for non-isotropic scattering in b) applying both NL (circlets/diamonds with transparent body) and HE (circlets/diamonds with coloured body) estimators. Different Doppler spreads, i.e. $B_\mu T_S = \{0.02, 0.05, 0.1\}$, are indicated in blue, green and black respectively. The NCRLBs are plotted as appropriately colour-coded dashed lines. It can be observed that the simulation results closely achieve the NCRLB, nonetheless the adhesive bias causes little deviations which appear constant over the depicted AoA regime.
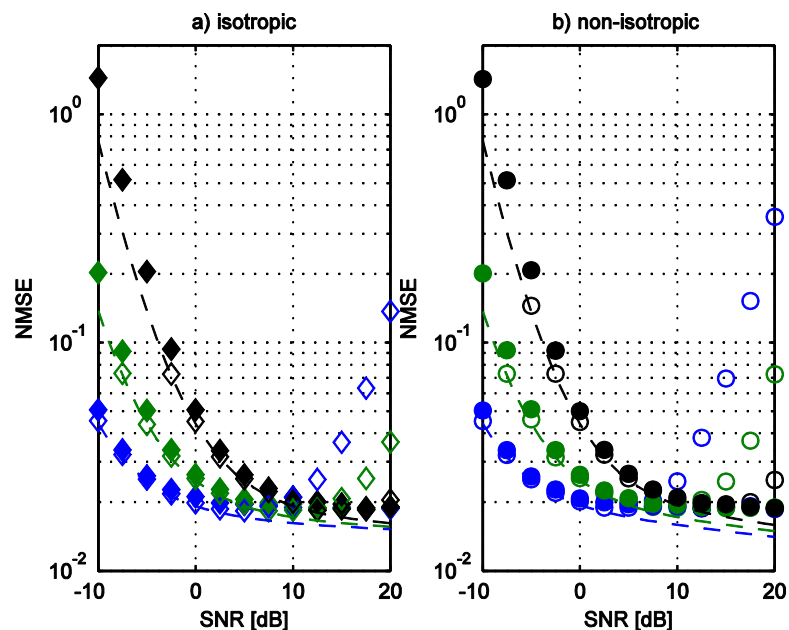
Figure 2.22: NMSE of the interference power estimates for
isotropic and non-isotropic scattering
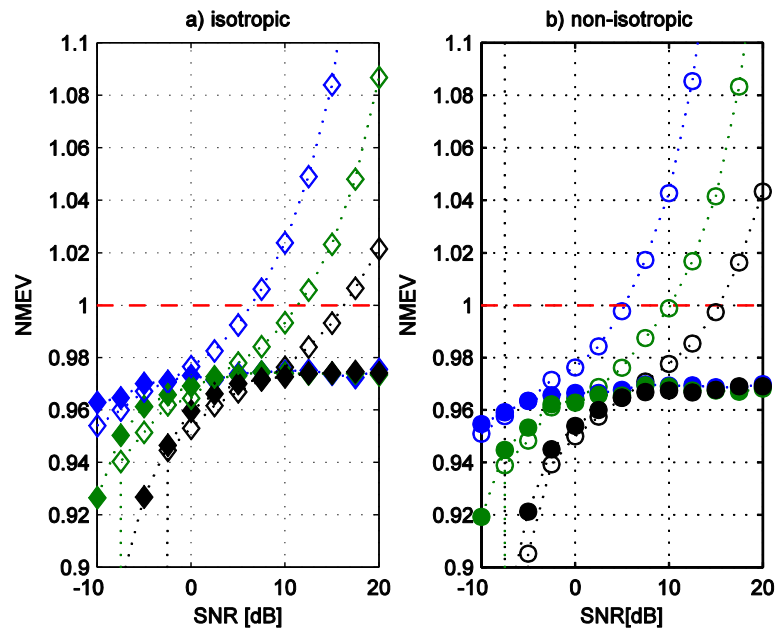
Figure 2.23: NMEV of the interference power estimates for isotropic and non-isotropic scattering
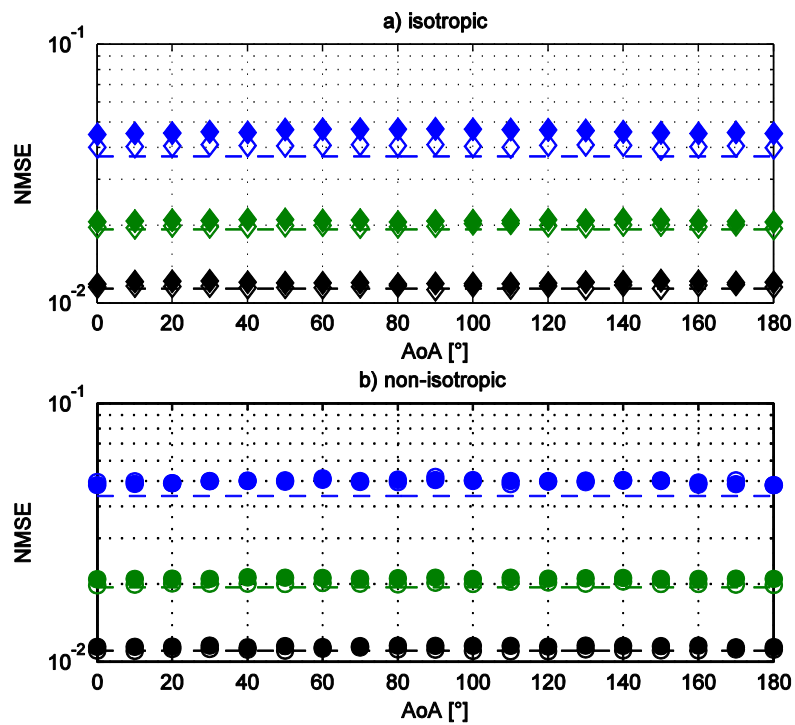
Figure 2.24: Interference power estimation performance vs. AoA
$(SNR = 10\ dB, K_R = 10\ dB)$

2.6.4 Power Ratio Estimation

Typically, power ratio estimations are the most important outputs of channel estimators as they often represent figures of merit used for link adaptations, thus solely looking at the power parameters may not be sufficient. Therefore, this section subsequently investigates the estimation performance of the power ratios, i.e. SNR and SIR; benchmarks are provided and the results are discussed. Again, two basic methods are compared – the one described in Section 2.4.1 which in the sequel is loosely denoted as NL method because of its nonlinear algorithmic and the one introduced in Section 2.4.2 which is loosely termed as heuristic estimation (HE) being developed in the original work presented in [6]. The evidence for the latter to be an ML solution under strictly bandlimited and flat fading conditions was found in [7] already.

2.6.4.1   SNR Estimation

Figure 2.25 depicts the jitter performance in terms of the NMSE of the SNR estimates at $K_R = \{0, 5, 10\}dB$ colour-coded in blue, green and black, respectively. Results for both isotropic and for non-isotropic scattering are indicated for the NL (circlets/diamonds with transparent body) and the HE (circlets/diamonds with coloured body) estimation method according to the applicable standard settings. The associated NCRLBs are indicated as appropriately colour-coded dashed lines. It was refrained from plotting the MEV since it is composed from S and N for which the respective MEVs were already indicated separately in Subsections 2.6.3.1 and 2.6.3.2. However, the simulation results are well aligned with the theoretical NCRLBs for isotropic and non-isotropic cases in the low to mid SNR regime. At higher SNR the results start to deviate from the NCRLBs which results from the increasing bias of the noise power in the higher SNR regime as indicated in Figure 2.20. Moreover, the NL estimation method earlier deviates from the NCRLB compared to the HE method since it suffers from a higher bias due to stability issues of the Newton-Raphson algorithm. In other words, the SNR estimation performance of NL and HE method is similar in the low to mid SNR regime and follows the NCRLB, thus the comparably improved performance in the high SNR regime and the lower computational complexity suggests resorting to the HE method for SNR estimation.

Figures 2.26 and 2.27 depict the SNR estimation performance in terms of the NMSE with respect to the AoA; results for isotropic and non-isotropic scattering applying both NL (circlets/diamonds with transparent body) and HE (circlets/diamonds with coloured body) estimators are depicted, respectively. Different Doppler spreads, i.e. $B_\mu T_S = \{0.02, 0.05, 0.1\}$, are indicated and the NCRLBs are plotted as appropriately colour-coded dashed lines according to the provided legend. Obviously, the simulation results

closely achieve the respective NCRLBs over the whole AoA regime for both estimation methods.
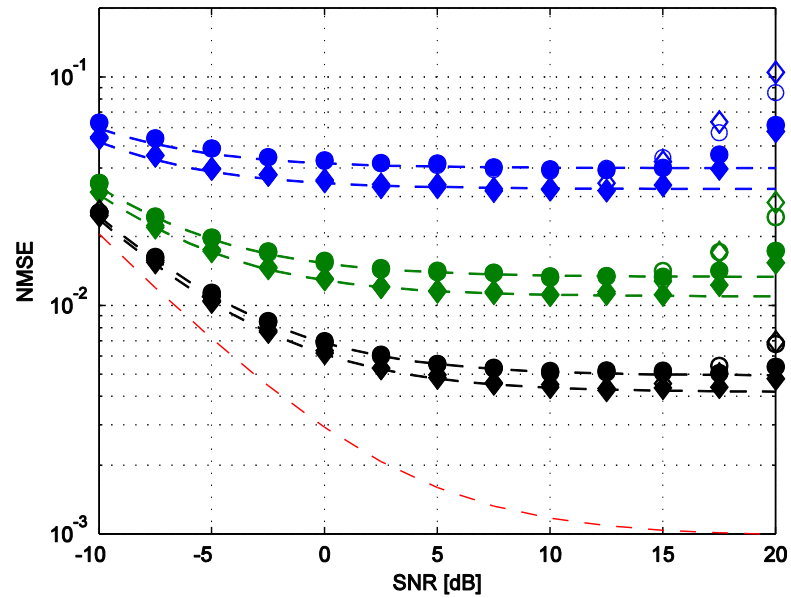
Figure 2.25: NMSE of the SNR estimates for
isotropic and non-isotropic scattering
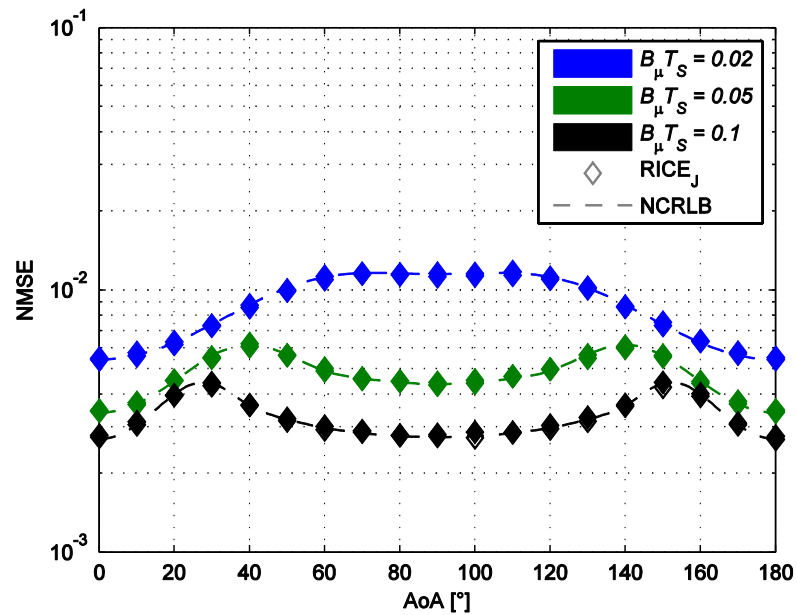
Figure 2.26: SNR estimation performance vs. AoA for
isotropic scattering ($SNR = 10\ dB$, $K_R = 10\ dB$)
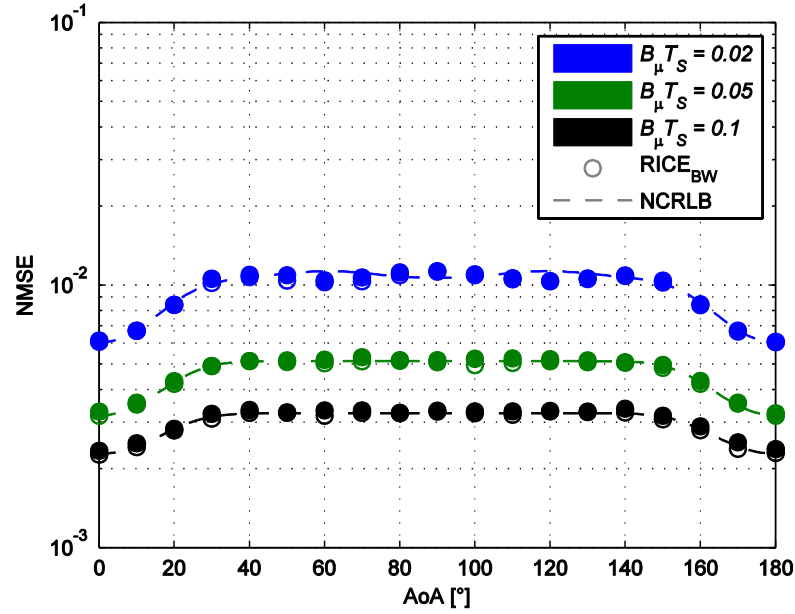
Figure 2.27: SNR estimation performance vs. AoA for non-isotropic scattering ($SNR = 10\ dB$, $K_R = 10\ dB$)

2.6.4.2 SIR Estimation

Figure 2.28 depicts the jitter performance in terms of the NMSE of the SIR estimates at $K_R = \{0, 5, 10\}dB$ colour-coded in blue, green and black, respectively. Analogously to above, results for both isotropic and for non-isotropic scattering are indicated for the NL (circlets/diamonds with transparent body) and the HE (circlets/diamonds with coloured body) estimation method according to the applicable standard settings. The associated NCRLBs are indicated as appropriately colour-coded dashed lines. Again, it was refrained from plotting the MEV since it is composed from S and I for which the respective MEVs were already indicated separately in the Subsections 2.6.3.1 and 2.6.3.3. The simulation results in general do not achieve the performance predicted by the theoretical NCRLBs for both isotropic and non-isotropic cases mainly due to the bias in the interference power estimation. It can be observed that the NL estimation results approach the respective NCRLB in the mid to high SNR region which is due to the vanishing interference bias in that region as depicted in Figure 2.23. At higher SNR the NL results start to deviate from the NCRLBs which results from the increasing bias of the interference power in the higher SNR regime. However, the SIR estimation performance of NL method is better than the performance of the HE method in the low to mid SNR regime; in the high SNR regime it is vice versa.

Figures 2.29 and 2.30 depict the SIR estimation performance in terms of the NMSE with respect to the AoA; results for isotropic and non-isotropic scattering applying both NL (circlets/diamonds with transparent body) and HE (circlets/diamonds with coloured

body) estimators are depicted, respectively. Different Doppler spreads, i.e. $B_\mu T_S = \{0.02, 0.05, 0.1\}$, are indicated and the NCRLBs are plotted as appropriately colour-coded dashed lines according to the provided legend.
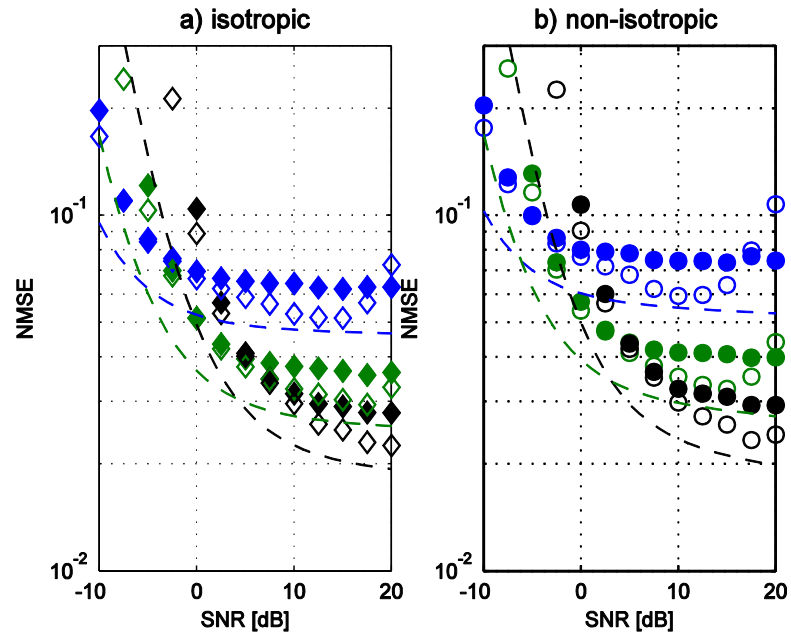
Figure 2.28: NMSE of the SIR estimates for
isotropic and non-isotropic scattering
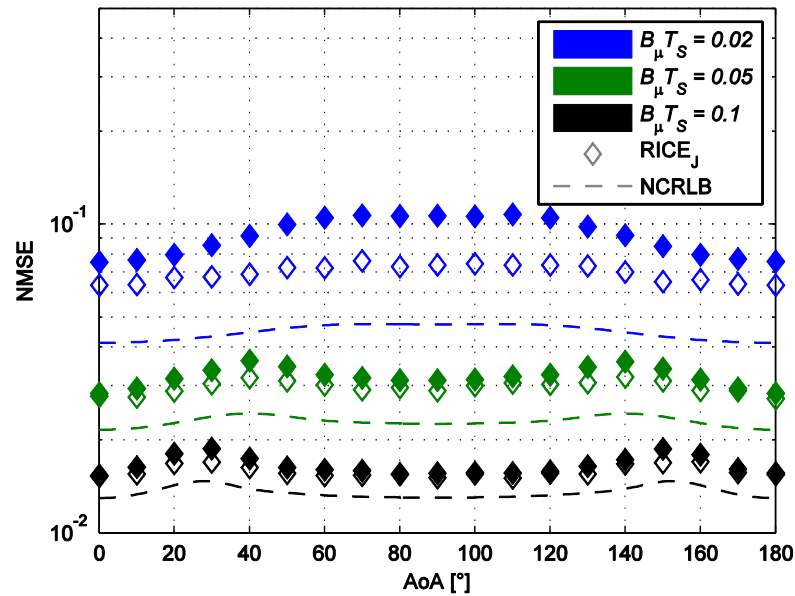
Figure 2.29: SIR estimation performance vs. AoA for
isotropic scattering ($SNR = 10\ dB$, $K_R = 10\ dB$)
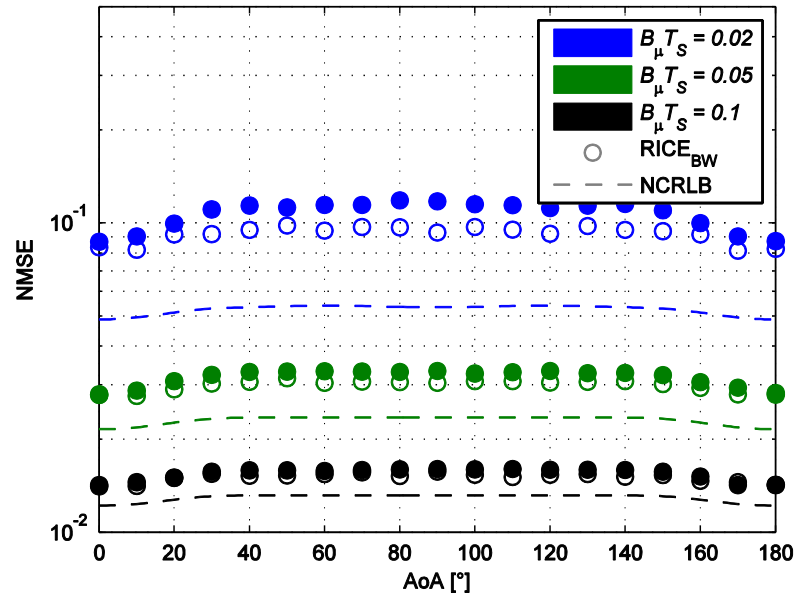
Figure 2.30: SNR estimation performance vs. AoA for
non-isotropic scattering ($SNR = 10\,dB$, $K_R = 10\,dB$)

Analogously to Figure 2.28, the simulation results provided in the Figures 2.29 and 2.30
do not achieve the respective NCRLBs over the whole AoA regime for both estimation
methods, whereas for the chosen simulation parameters the HE method in general per-
forms worse. However, towards the edges, i.e. towards the positive and negative maxi-
mum Doppler spread, the comparably better performance of the NL method vanishes.

2.7 Stability and Accuracy Issues of the Nonlinear Estimation Method

According to the simulation results presented in Section 2.6 it is obvious that the NL
estimation method encounters some stability issues. Based on the standard settings as
outlined in Subsection 2.6.1 investigations on this performance issue are presented in
the following. Furthermore the NL method requires the knowledge of the spectral chan-
nel shape, thus some considerations about its sensitivity on discrepancies of the channel
model with the true channel are provided.

2.7.1 Performance Loss by Mismatching Filter Models

As already mentioned, the NL method presumes the channel model to be exactly
known. However, subsequent performance figures investigate the influence of an inac-

curate knowledge of the channel model. More specifically, simulations were performed using the isotropic channel model whereas the algorithm assumes the non-isotropic channel model to apply. All other simulation settings follow the standard settings.

The Figures 2.31 and 2.32 compare the jitter performance in terms of the NMSE of the SNR estimates at $K_R = \{0, 5, 10\}dB$ colour-coded in blue, green and black, respectively for isotropic channel conditions with a perfectly known (diamonds) and a not perfectly known (stars) scattering model, respectively. NCRLBs are indicated using appropriately colour-coded dashed lines – the red dashed line represents the NCRLB for SNR estimates under AWGN conditions. Moreover, the standard settings apply. It can clearly be seen that the SNR and SIR estimation performance decreases in the mid to higher SNR regime; surprisingly, the SIR estimation performance is slightly better in the mid SNR regime, which by close inspection follows from a little shift in the bias behaviour along the SNR axis.

The Figures 2.33 and 2.34 compare the SNR and SIR estimation performance for different Doppler spreads, i.e. $B_\mu T_S = \{0.02, 0.05, 0.1\}$, for isotropic channel conditions with a perfectly known (diamonds) and a not perfectly known (stars) scattering model, respectively. The applicable colour-coding is indicated in the plotted legends; besides that, the standard settings apply. For a Doppler spread of $B_\mu T_S = 0.02$ a strong degradation of the SIR estimation performance is observed; SNR estimates do not exhibit significant performance losses.
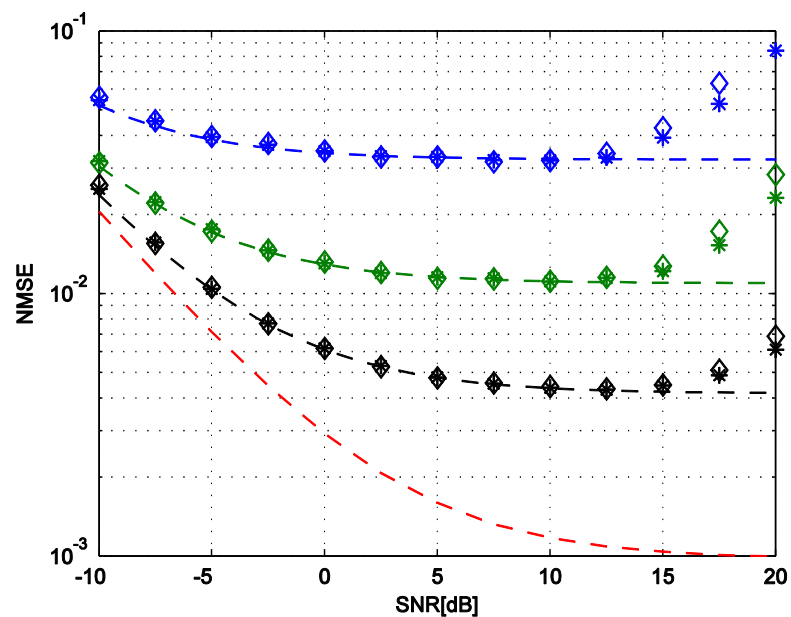
Figure 2.31: NMSE of the SNR estimates for
incorrectly known scattering models
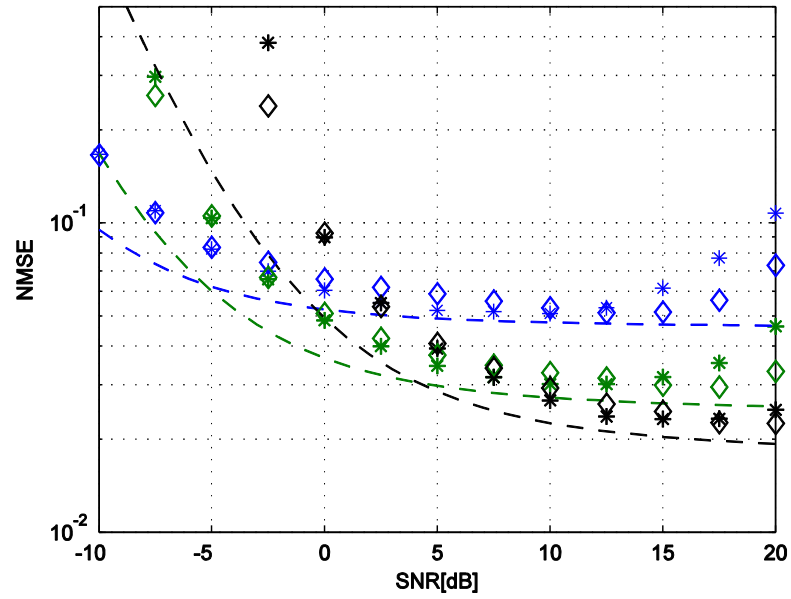
Figure 2.32: NMSE of the SIR estimates for
incorrectly known scattering models
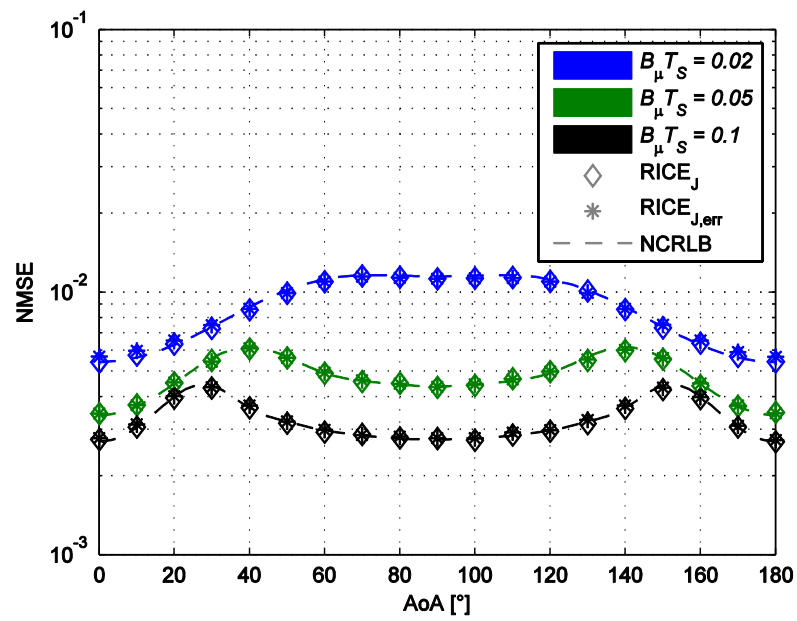
Figure 2.33: SNR estimation performance vs. AoA for isotropic scattering
at unknown spectral channel shape ($SNR = 10\ dB$, $K_R = 10\ dB$)
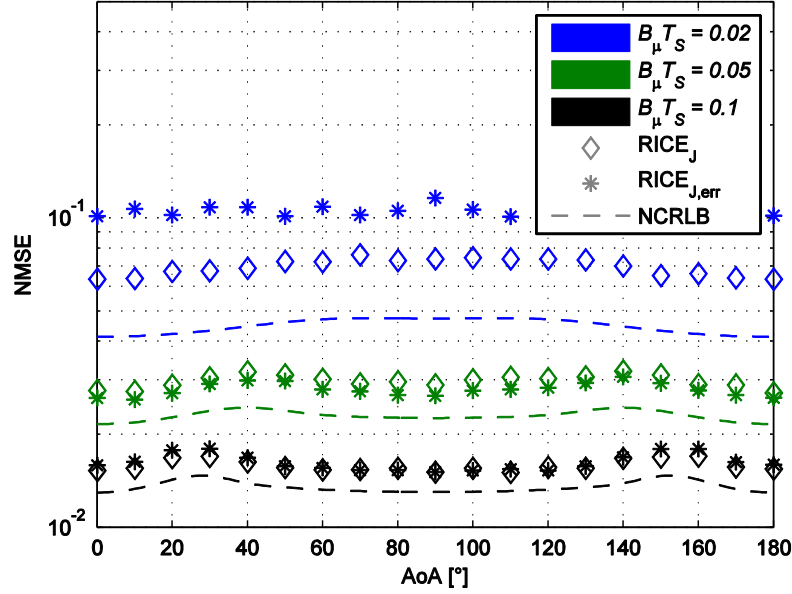
Figure 2.34: SIR estimation performance vs. AoA for isotropic scattering
at unknown spectral channel shape ($SNR = 10\ dB$, $K_R = 10\ dB$)

2.7.2 Stability and Performance due to Matrix Inversion

A central and critical issue of the Newton-Raphson method is matrix inversion of the matrix **J** according to (2.52). As already mentioned, LU and QR decomposition are often suggested in the literature to prevent from singularities [25, pp. 347-393] [29, pp. 80-89]. Since simulations in this thesis were carried out with MATLAB, the implemented matrix inversion functionality was used as a standard, which in some cases generated singularity warnings when performing the mentioned inversion. Since MATLAB uses high precision number formats, those warnings were not an issue. Resorting to QR and LU decomposition avoided those singularity warnings, but did not improve the simulation results. Considering the special case of matrix inversion required for the NL estimation algorithm, i.e. a regular 2×2 matrix, the inversion may also be computed as [31, 152-197].

$$\mathbf{J}^{-1} = \begin{bmatrix} J_{1,1} & J_{1,2} \\ J_{2,1} & J_{2,2} \end{bmatrix}^{-1} = \frac{1}{J_{1,1} \cdot J_{2,2} - J_{1,2} \cdot J_{2,1}} \cdot \begin{bmatrix} J_{2,2} & -J_{1,2} \\ -J_{2,1} & J_{1,1} \end{bmatrix}. \tag{2.94}$$

Applying (2.94) also prevents from singularity issues, but does neither improve the simulation performance. However, for practical implementations the inversion outlined in (2.94) could help to tackle the stability issue by simple means.

2.8   Conclusion

Considering the analytic framework established for the Rician channel and the estimation framework derived, an ML estimator for carrier and power parameters implements the following tasks in consecutive order:

1. Carrier frequency and phase recovery,
2. Doppler spread estimation,
3. Estimation of the power parameters (signal/interference/noise power).

A suitable DA estimator for frequency estimation and correction is applied, followed by a carrier phase recovery. Appropriate Doppler spread estimators, such as those published in [1], [6], [26] and [27], delivering the Doppler spread and hence the region in the periodogram occupied by noise power only is the next step. From there the power estimates and their respective ratios can be established using the nonlinear (NL) method described in 2.4.1 or its simplified version (HE method) described in 2.4.2. However, comparing NL and HE methods suggests that resorting to the simplified algorithm might provide benefits in terms of complexity and stability, because the NL method is far more complex than the HE method and especially at low Doppler spreads the former suffers from an inaccurate knowledge of the channel spectral model. Furthermore, the performance gain achievable with the NL method for SIR estimates is rather low and limited to the mid SNR region; for SNR estimates no performance gain could be observed. However, in the high SNR region the NL estimator in general performs worse than the HE estimator.

3 Unconventional Channel Estimation on Multibeam Satellite Links

After completing his dissertation [1], the author of this thesis continued investigating parameter estimation methods on multibeam satellite channels. Therefrom a novel and unconventional estimation method was developed in collaboration with Prof. Wilfried Gappmair and Barbara Süsser-Rechberger which was identified by Graz University of Technology as a potential key technology for satellite communication systems and hence a patent filing process was triggered in 2013. Subsequently, a brief description of the technology is provided in adaptation of the original work prepared in [30]. It is refrained from extensively quoting the original unpublished work hereafter; the author holds the permission to fully or partially reprint its contents for this thesis.

3.1 Preface

Studies based on achievements published in [32]-[35] were carried out in the context of the SatNEx III CoO1 project of ESA [36]-[41]. Throughout this ESA project an extensive literature review was pursued in the first phase [36]. However, traditional estimation concepts for multibeam satellite channels were available at this time only [30] and the publications [42] and [43] originating from that study elaborated on the advances achieved in that context. In [1] the original work was summarized and a deterministic relationship of the interference components on the link postulated. With a novel concept, denoted as "Location-Aware Channel Estimation", the authors could demonstrate in [1], [44] and [45] that, by considering the antenna model (pattern) and the user terminal position to be known, the estimation performance of classical approaches can significantly be improved. In a student project supervised by the author of this thesis in [46], dilutions of the knowledge of the user position were investigated and found to have a less significant impact. Some findings of [1] and [46] were published in [44] and [45]. So far efforts were focused on the minimization of the detrimental interference on the performance of channel estimations, thus it was tried to maximize the SNIR.

The work presented hereafter follows a significantly different approach. Guided by the limitations found in the work previously described, the detrimental interference is tackled in a novel way by generically constructing a unique word for estimations based on the knowledge of the user terminal position and the antenna model (pattern). The idea

behind that approach is to change the role of the interference in the system from a detrimental noise to a helpful signal.

In the sequel the channel model for multibeam satellite links will briefly be introduced in Section 3.2, followed by the novel estimation concept in Section 3.3. Performance figures and benchmarks in comparison to classical approaches will be presented in Section 3.4 followed by concluding remarks in Section 3.5. For more details on the multibeam scenario as well as on state-of-the-art estimation methods the interested reader is referred to [1, Chapter 3] and references therein.

3.2 The Multibeam Satellite Channel Model

The considered multibeam satellite channel consists of a number of K spot beams which form the user cells (Figure 3.1 [1] sketches the forward link); each of which is capable to serve one user at a time, thus K users can be served simultaneously. These K beams (an illustration of a footprint is provided in Figure 3.2 [1]) are generated by N feeds, $N \geq K$, which are considered to be operated on the same frequency (full frequency reuse). This aggressive frequency reuse boosts the spectral efficiency at the expense of high interference. Joint beamforming and precoding techniques can mitigate this sort of impairment, but they require accurate and timely channel estimates in order to perform well. It is to be noticed that the system performance in terms of throughput can be increased by applying beamforming and precoding in the feed space, thus channel estimation must be implemented accordingly [43].

The signal model for the forward link in the feed signal subspace is given as

$$\mathbf{y} = \mathbf{H} \cdot \mathbf{x} + \mathbf{n}, \tag{3.1}$$

where $\mathbf{H}$ is the $K \times N$ channel matrix in the feed signal space, $\mathbf{y} = (y_1, y_2, \dots, y_K)^T$, and $\mathbf{x} = (x_1, x_2, \dots, x_N)^T$; the superscript T denotes the transpose. The channel matrix $\mathbf{H} = \mathbf{W} \cdot \mathbf{G} \cdot \mathbf{D}$, where [36]

- $\mathbf{W}$ is the $K \times K$ diagonal fading matrix on the downlink; the entry (m, m) accounts for the gain of user terminal m,
- $\mathbf{G}$ represents the $K \times N$ feeder matrix whose entries (m, n) represent the gain between user signal path m and antenna feed n, and

- **D** is a $N \times N$ matrix accounting for effects occurring on the feeder link and in the on-board repeater chain; as mentioned above, **D** may be regarded as ideal considering a hybrid space ground processing concept [43].
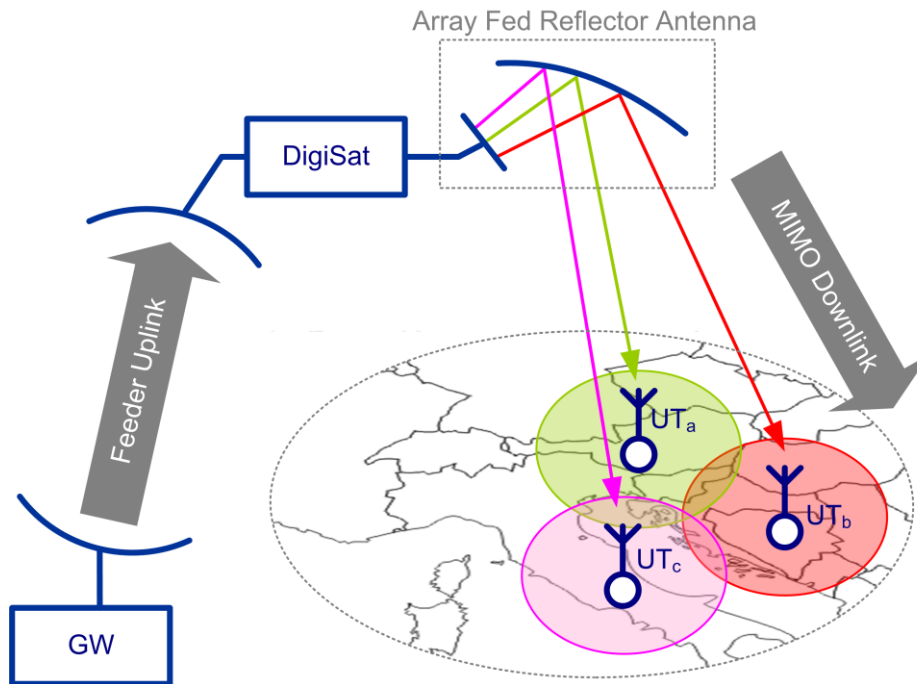
Figure 3.1: Forward link architecture with three outlined cells[3]
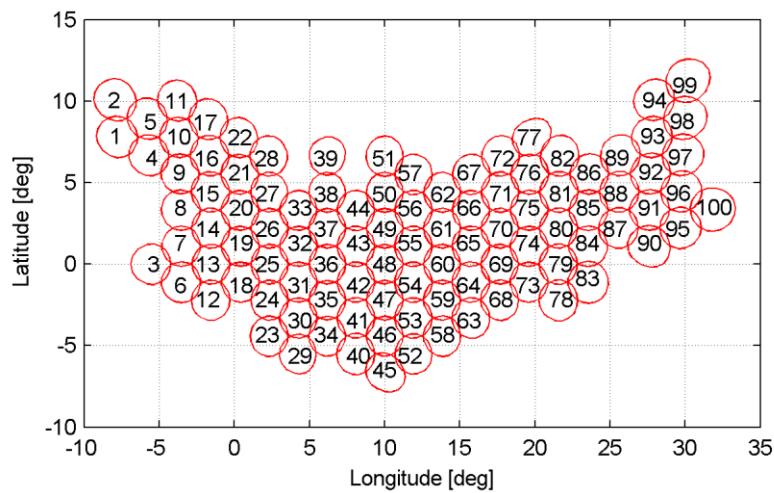
Figure 3.2: Footprint of the antenna beams with full frequency reuse

Figure 3.3 sketches the multibeam satellite forward link to the mth user terminal, which is related to the mth row of the channel matrix **H**; hence, $\mathbf{h}_m = \left(h_{m,1}, h_{m,2}, \ldots, h_{m,N} \right)$,

---

[3] The map depicted in Figure 3.1 is used and modified from source: http://d-maps.com/carte.php?lib=europe_map&num_car=2233&lang=en (2011-09-27).

$m = 1, 2, \ldots, K$, holds N complex values describing the respective channel effects such as feed radiation pattern, atmospheric fading, slanted path loss, and receive antenna gain [43].
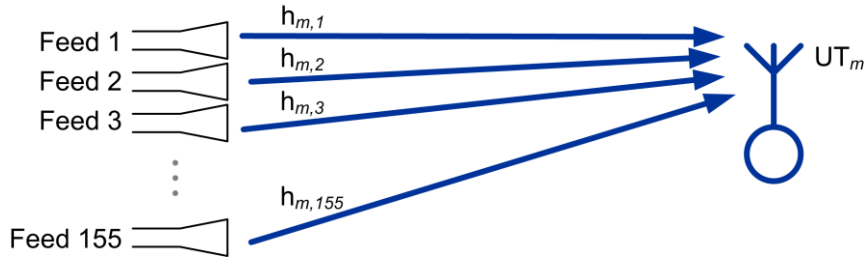
Figure 3.3: Satellite downlink for the m-th user terminal

In order to estimate $\mathbf{H}$, data-aided channel estimation requires non-precoded unique words to be foreseen in the physical layer framing structure [36]. These identifier sequences $\mathbf{c}_m = (c_{m,1}, c_{m,2}, \ldots, c_{m,L})$, $m = 1, 2, \ldots, N$, of length L must be unique for each feed; their desired properties, like orthogonality and linear independence, are discussed in due detail in [1]. With $\mathbf{C} = (\mathbf{c}_1, \mathbf{c}_2, \ldots, \mathbf{c}_N)^T$ and $\mathbf{X} = (\mathbf{x}_1, \mathbf{x}_2, \ldots, \mathbf{x}_{L_x})$, where L_x is the payload data length, as shown in Figure 3.4, where $L \ll L_x$.
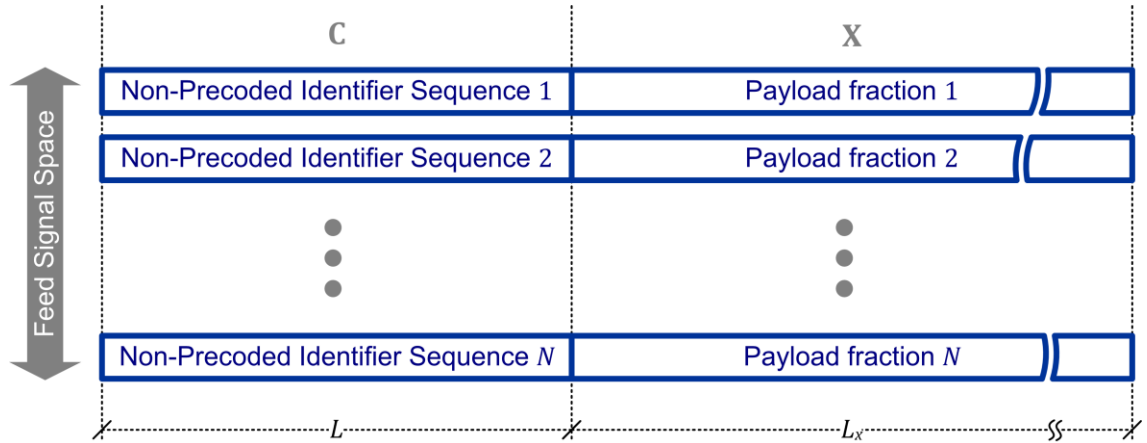
Figure 3.4: Physical layer framing on the multibeam satellite forward link

Concluding the signal model for the forward link with focus on the identifier sequences only, as required for channel estimation, then it becomes

$$\mathbf{Y} = \mathbf{H} \cdot \mathbf{C} + \mathbf{N}, \tag{3.2}$$

where $\mathbf{Y} = (\mathbf{y}_1, \mathbf{y}_2, \ldots, \mathbf{y}_L)$.

Considering the received sequence at the kth user terminal, we have

$$\mathbf{y}_k = \mathbf{h}_k \cdot \mathbf{C} + \mathbf{n}_k, \tag{3.3}$$

with $\mathbf{y}_k = (y_{k,1}, y_{k,2}, \dots, y_{k,L})$, $\mathbf{h}_k = (h_{k,1}, h_{k,2}, \dots, h_{k,N})$ and $\mathbf{n}_k$ being the noise sequence. In this context, $\mathbf{h}_k$ denotes the channel matrix (vector) between the multibeam antenna (with N feeds) of the satellite and the k-th user terminal; each entry in $\mathbf{h}_k$ is a complex value composed as follows:

$$h_{k,n} \,|_{\,n \in \{1,2,\dots,N\}} = a_{k,n} \cdot e^{j \cdot \theta_{k,n}} \cdot a_{k,0} \cdot e^{j \cdot \theta_{k,0}}, \tag{3.4}$$

where

- $a_{k,n}$ and $\theta_{k,n}$ account for the n-th feed gain and phase shift, respectively, induced by the multibeam antenna with respect to the position of the k-th user.
- $a_{k,0}$ and $\theta_{k,0}$ account for the gain (inverse attenuation) and phase shift induced by the physical link between the satellite and user terminal k.

By inspection of (3.4) it becomes obvious that all signals emitted by the satellite towards user terminal k travel on the same physical path, thus encounter the same impairments, so the term $a_{k,0} \cdot e^{j \cdot \theta_{k,0}}$ is identical for all signal components. By forming the ratio

$$\beta_{k,n_1,n_2} \Big|_{\,n_1,n_2 \in \{1,\dots,N\}} = \frac{h_{k,n_1}}{h_{k,n_2}} = \frac{a_{k,n_1} \cdot e^{j \cdot \theta_{k,n_1}}}{a_{k,n_2} \cdot e^{j \cdot \theta_{k,n_2}}} \tag{3.5}$$

the physical path cancels out. Therefore, β_{k,n_1,n_2} depends only on the user terminal position with respect to the properties given by the antenna model. This observation was exploited in [1], [44] and [45] to improve the channel estimation by knowing the user location.

3.3   Unconventional Channel Estimation

The term *Unconventional Channel Estimation* is related to the way of thinking which led to this novel estimation approach; the construction of a generic unique word by applying knowledge about the antenna pattern and the user terminal position which is then used for channel estimation, is completely different to the state-of-the-art technologies, although the novel concept might be easy understandable once considered. The novel idea, termed LAUCO (for *Location-Aware Unique Word Construction*) below, significantly differs from previous approaches. Instead of mitigating interference originating from the unique words emitted by other feeds, the method modifies the deterministic relationships so that the interference – in the sequel denoted as multiple access interference (MAI) – contributes in a constructive manner to the useful signal component.

The main idea is to consider the interference as part of the signal by constructing a generic unique word used for data-aided estimation. This is achieved by the set of unique words given in $\mathbf{C}$ and the *deterministic* relationships postulated in (3.5). This yields

$$\mathbf{c}_k^{LA} = \boldsymbol{\beta}_{k,n_x} \cdot \mathbf{C}, \tag{3.6}$$

where $\boldsymbol{\beta}_{k,n_x} = \left(\beta_{k,1,n_x}, \beta_{k,2,n_x}, \ldots, \beta_{k,N,n_x}\right)$, n_x denotes the index of the reference feed which should preferably be chosen as the strongest one from the viewpoint of user terminal k, and the superscript LA indicates the required location awareness. In this respect, the data-aided estimation performs as

$$\hat{\zeta}_k^{LA} = \mathbf{y}_k \cdot \mathbf{c}_k^{LA^H}, \tag{3.7}$$

with $\hat{\zeta}_k^{LA}$ as the total estimate and H denoting the Hermitian transpose. By close inspection of the total estimate, we see that

$$E\left[\hat{\zeta}_k^{LA}\right] = \mathbf{h}_k \cdot \mathbf{C} \cdot \mathbf{c}_k^{LA^H}, \tag{3.8}$$

where $E[\cdot]$ denotes expectation. Substituting (3.6) into (3.8) yields

$$E\left[\hat{\zeta}_k^{LA}\right] = \mathbf{h}_k \cdot \mathbf{C} \cdot \mathbf{C}^H \cdot \boldsymbol{\beta}_{k,n_x}^H, \tag{3.9}$$

which, by applying (3.5), can be further extended to

$$E\big[\hat{\zeta}_k^{LA}\big] = h_{k,n_x} \cdot \boldsymbol{\beta}_{k,n_x} \cdot \mathbf{C} \cdot \mathbf{C}^H \cdot \boldsymbol{\beta}_{k,n_x}^H. \tag{3.10}$$

With $\lambda_{k,n_x} = \boldsymbol{\beta}_{k,n_x} \cdot \mathbf{C} \cdot \mathbf{C}^H \cdot \boldsymbol{\beta}_{k,n_x}^H$ we have

$$E\big[\hat{\zeta}_k^{LA}\big] = h_{k,n_x} \cdot \lambda_{k,n_x}. \tag{3.11}$$

Given the total estimate in (3.7), it straightforwardly follows from (3.11) that

$$\hat{h}_{k,n_x} = \frac{\hat{\zeta}_k^{LA}}{\lambda_{k,n_x}}. \tag{3.12}$$

The estimate of the channel matrix (vector) can finally be obtained as

$$\hat{\mathbf{h}}_k = \boldsymbol{\beta}_{k,n_x} \cdot \hat{h}_{k,n_x}. \tag{3.13}$$

3.4   Simulation Results

Simulations proving the capability of the LAUCO concept are provided within this section. The corresponding results are based on the same antenna model and link settings as those presented in [1], [36]-[46]. However, after outlining the simulation settings in Subsection 3.4.1, the results presuming ideal knowledge of the user terminal position are presented in Subsection 3.4.2 and simulations presuming inaccurate (diluted) knowledge of the user position are presented in Subsection 3.4.3. All simulation results presented for LAUCO are benchmarked with simulation results achieved by state-of-the-art methods [1], [36]-[43] and those of the recently introduced *Location-Aware Channel Estimation* (LACE) concept [1], [44]-[46].

3.4.1 General Simulation Settings

The *antenna model* provided by ESA for the Satellite Communication Network of Experts III Call of Order I project, partially published in [1], [36]-[43], is used as a baseline for the simulations. The forward link is a symbol-synchronous multibeam satellite link with hybrid space-ground processing, where the digital feeder uplink is considered to be ideal. The scenario foresees $N = 155$ feeds forming $K = 100$ beams (cells), thus being able to serve $K = 100$ users at a specific time slot. Full frequency reuse and a fixed satellite service are presumed. Results for a single user terminal are presented whose position is fixed for all simulation experiments.

Three types of non-precoded unique words (also denoted as identifier sequences) are simulated:

- Orthogonal (Hadamard) sequences of length $L = 256$
- Quasi-orthogonal and linearly-independent sequences with $L = 156$
- Quasi-orthogonal and linearly-dependent sequences with $L = 63$

Classical and LACE-based simulations with quasi-orthogonal and linearly-independent sequences apply the (Moore-Penrose) pseudo-inverse for channel estimation, quasi-orthogonal and linearly-dependent sequences require correlation-based operations instead. For orthogonal sequences both methods can be used as they provide the same result, both from a theoretical and a practical point of view [1], [42].

(Normalized) Cramer-Rao Lower Bounds ((N)CRLBs) are provided for benchmarking. It is to be noticed that the provided bounds refer to classical estimation approaches with orthogonal non-precoded unique words.

3.4.2 Ideal Knowledge of the User Position

Simulation results presented in this Subsection assume ideal knowledge the user position and, hence, of the vector $\boldsymbol{\beta}_{k,n_x}$. The accuracy of the estimates is examined in terms of the complex error vector decomposed in its amplitude and phase component, for which the (normalized) mean square error ((N)MSE) is provided. The presented results compare classical methods and LACE with LAUCO

- for orthogonal non-precoded unique words of length $L = 256$ symbols in Figure 3.5 and Figure 3.6,
- for quasi-orthogonal and linearly-independent non-precoded unique words of length $L = 156$ symbols in Figure 3.7 and Figure 3.8 and
- for quasi-orthogonal and linearly-dependent non-precoded unique words of length $L = 63$ symbols in Figure 3.9 and Figure 3.10.

For all mentioned, figures subplots a), b) and c) depict results for the classical method, for LACE and for LAUCO, respectively; the results for the strongest feed are plotted as black line and the remaining feed signals are grey. The (N)CRLB (red dashed line) is used as a benchmark and refers to the strongest feed with respect to the classical estimation method [42]. The Signal-to-Noise Ratio (SNR) with index 1 on the abscissa of the performance plots indicates that it refers to the signal power of the strongest feed signal.

The diagrams reveal that the LAUCO outperforms the present estimation methods for all kinds of unique word sequences. LAUCO estimates all feed signals at virtually the same performance which holds also true for LACE, but LAUCO does neither exhibit the drawback of error amplification (Figure 3.7 and Figure 3.8) nor does it suffer from a jitter floor (Figure 3.9 and Figure 3.10). Moreover, LAUCO exhibits a significantly improved performance in comparison to the benchmark (N)CRLB; for the given satellite channel model this results in an estimation gain beyond 5 dB. For practical systems, this extra performance margin might be invested into an increased accuracy and/or into a reduced unique word length.
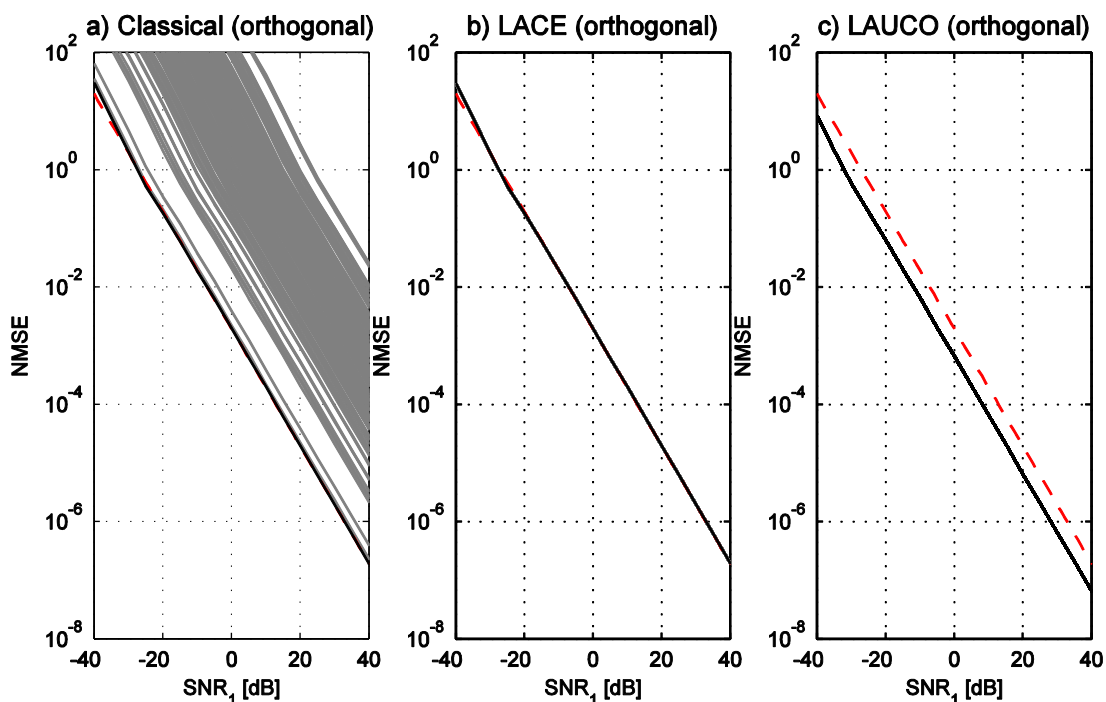
Figure 3.5: Estimation performance in terms of the amplitude NMSE
for orthogonal unique words ($L = 256$)
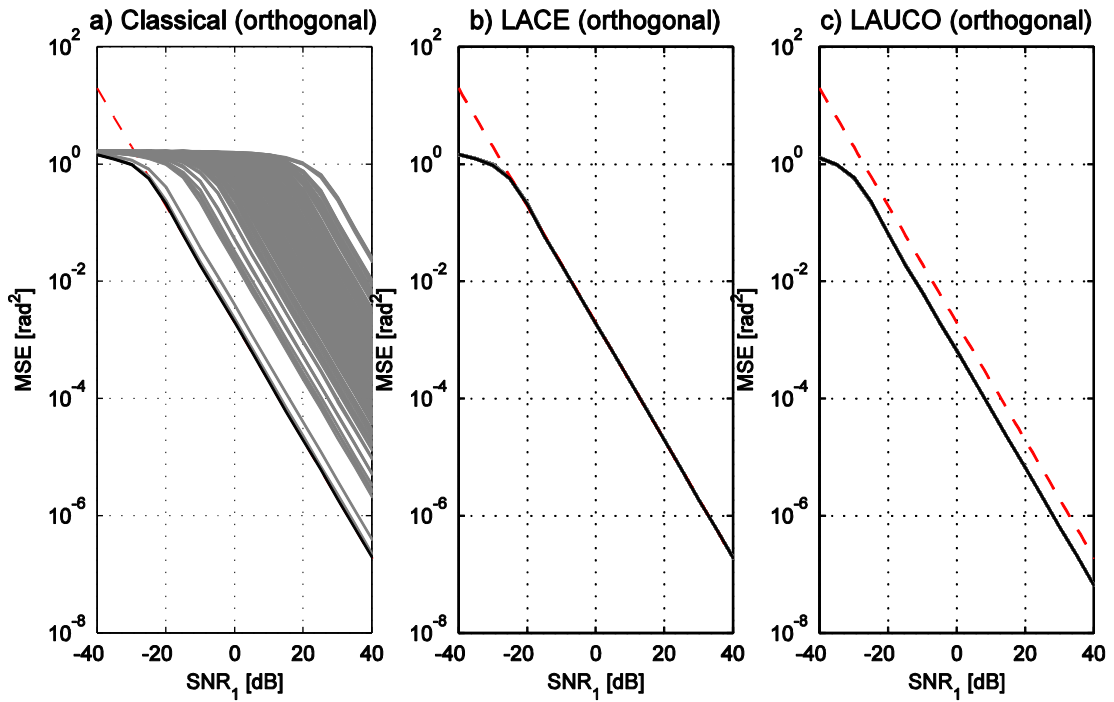
Figure 3.6: Estimation performance in terms of the phase MSE
for orthogonal unique words ($L = 256$)
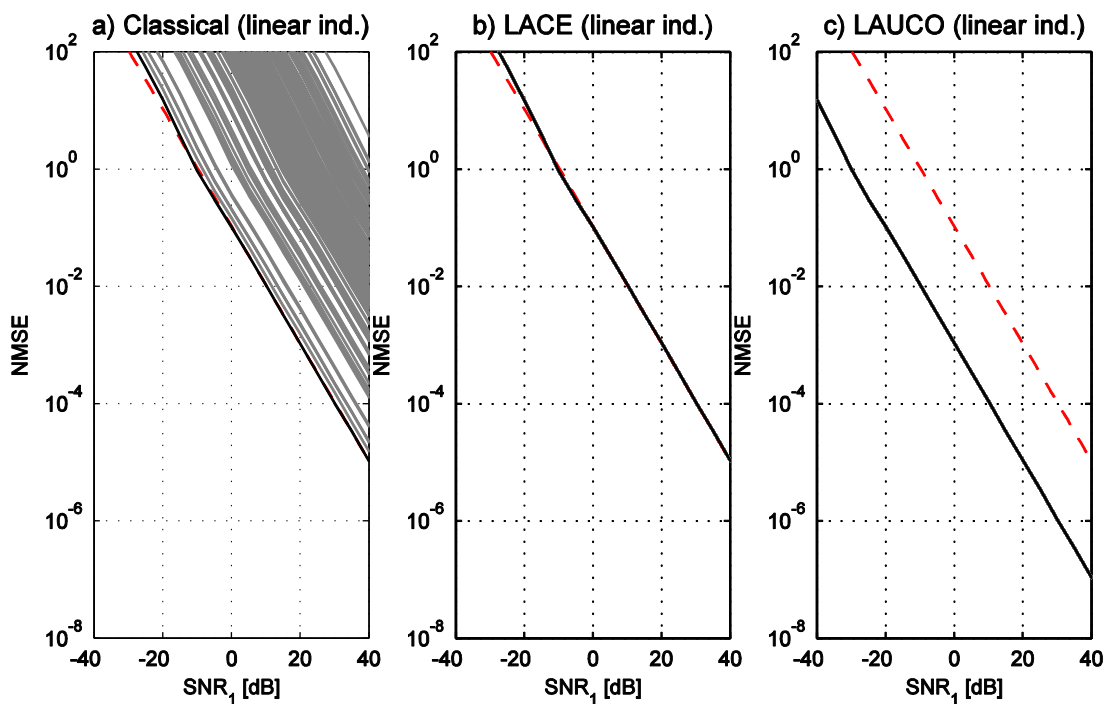
Figure 3.7: Estimation performance in terms of the amplitude NMSE
for quasi-orthogonal and linear independent unique words ($L = 156$)
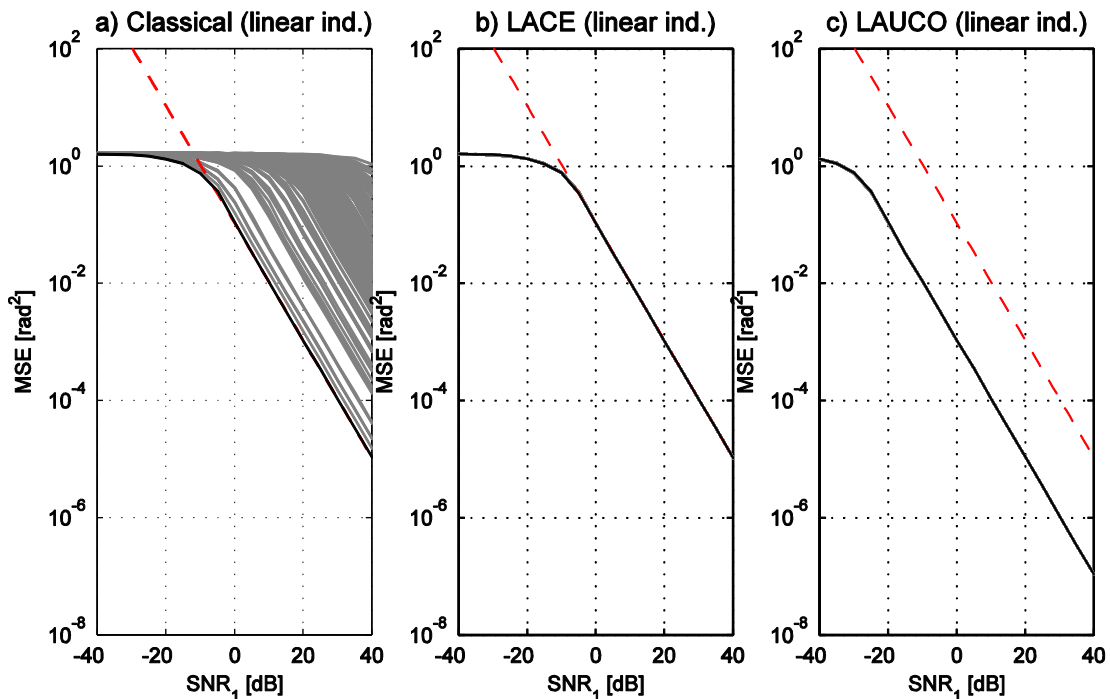
Figure 3.8: Estimation performance in terms of the phase MSE for quasi-orthogonal and linear independent unique words ($L = 156$)
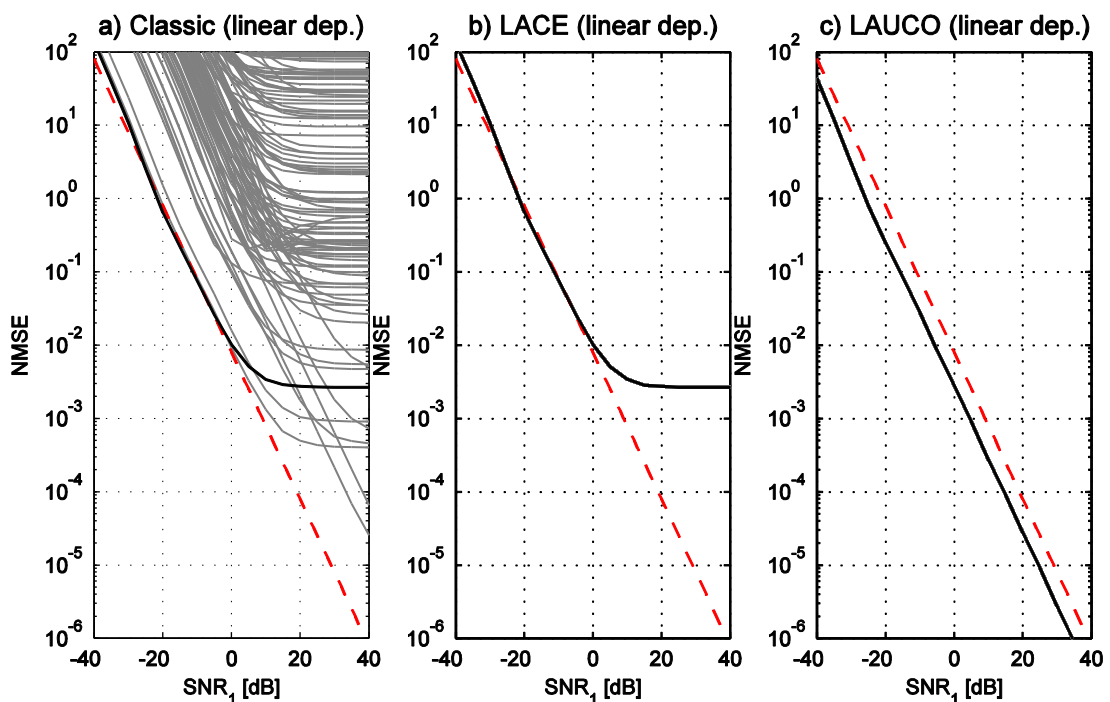
Figure 3.9: Estimation performance in terms of the amplitude NMSE for quasi-orthogonal and linearly dependent unique words ($L = 63$)
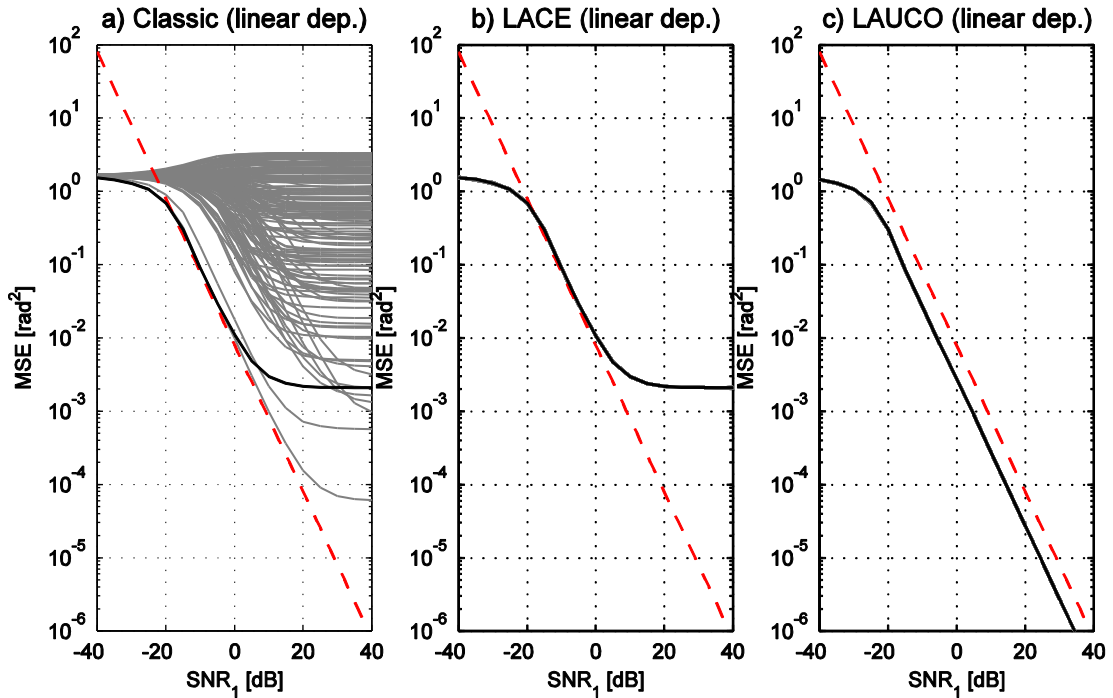
Figure 3.10: Estimation performance in terms of the phase MSE for quasi-orthogonal and linearly dependent unique words ($L = 63$)

3.4.3 Diluted Knowledge of the User Position

Simulation results presented in this subsection assume a diluted (inaccurate) knowledge of the user position and, hence, of the vector $\boldsymbol{\beta}_{k,n_x}$. The channel estimation accuracy is examined in terms of the NMSE of the amplitude component of the complex error vector. The performance of LAUCO is depicted

- for orthogonal non-precoded unique words of length $L = 256$ symbols in Figure 3.11,
- for quasi-orthogonal and linearly-independent non-precoded unique words of length $L = 156$ symbols in Figure 3.12 and
- for quasi-orthogonal and linearly-dependent non-precoded unique words of length $L = 63$ symbols in Figure 3.13.

For all mentioned figures, subplots a) and b) depict results for a *dilution of user positioning precision* (DUPP) of the LAUCO approach by 100 m and 10 km, respectively; the DUPP values provide a statistical measure of positioning uncertainty modelled by a circular two-dimensional Gaussian random distribution with a variance of 100/3 m and 10/3 km, respectively. The results for the strongest feed are plotted as black line and the remaining feed signals are grey. The (N)CRLB (red dashed line) is used as a benchmark and refers to the strongest feed with respect to the classical estimation method [42]. The

SNR with index 1 on the abscissa of the performance plots indicates that it refers to the signal power of the strongest feed signal. No performance figures are provided for the phase at this stage as this would require additional assumptions on the antenna size and the baud rate of the satellite system.

The Figures 3.11-3.13 show that DUPP impairs the accuracy of the LAUCO concept. Given modern positioning systems with their typical accuracies of a few meters, DUPP should not be a big problem in general. However, given the performance figures of LACE in [46] it is obvious that LAUCO performs better than LACE at a given DUPP. Comparing the LAUCO performance to the results presented for the classical methods in Subsection 3.4.2, it is obvious that LAUCO may tolerate a high DUPP.
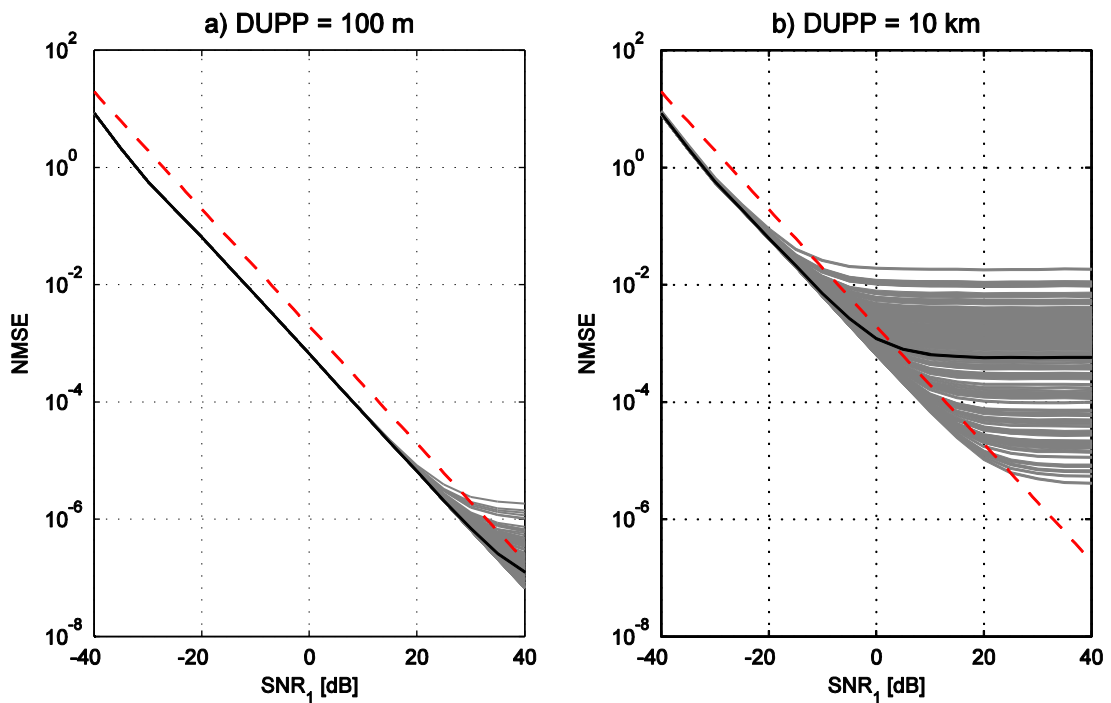
Figure 3.11: Estimation performance in terms of the amplitude NMSE
using orthogonal unique words at given DUPP
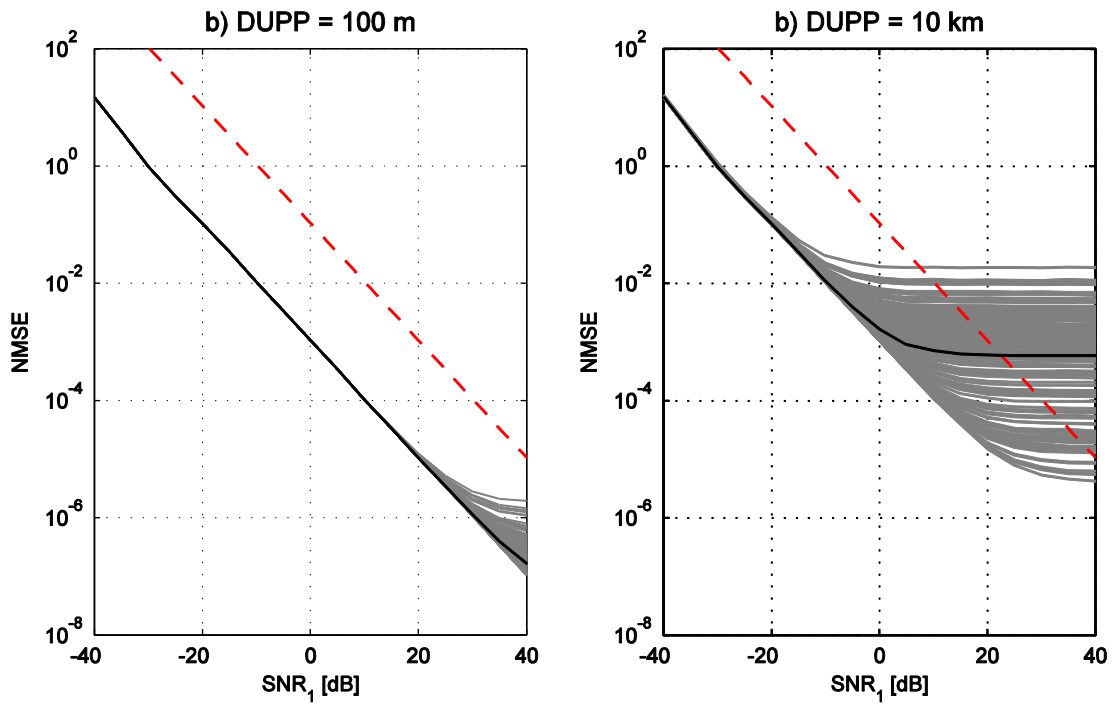
Figure 3.12: Estimation performance in terms of the amplitude NMSE using quasi-orthogonal and linearly independent unique words at given DUPP
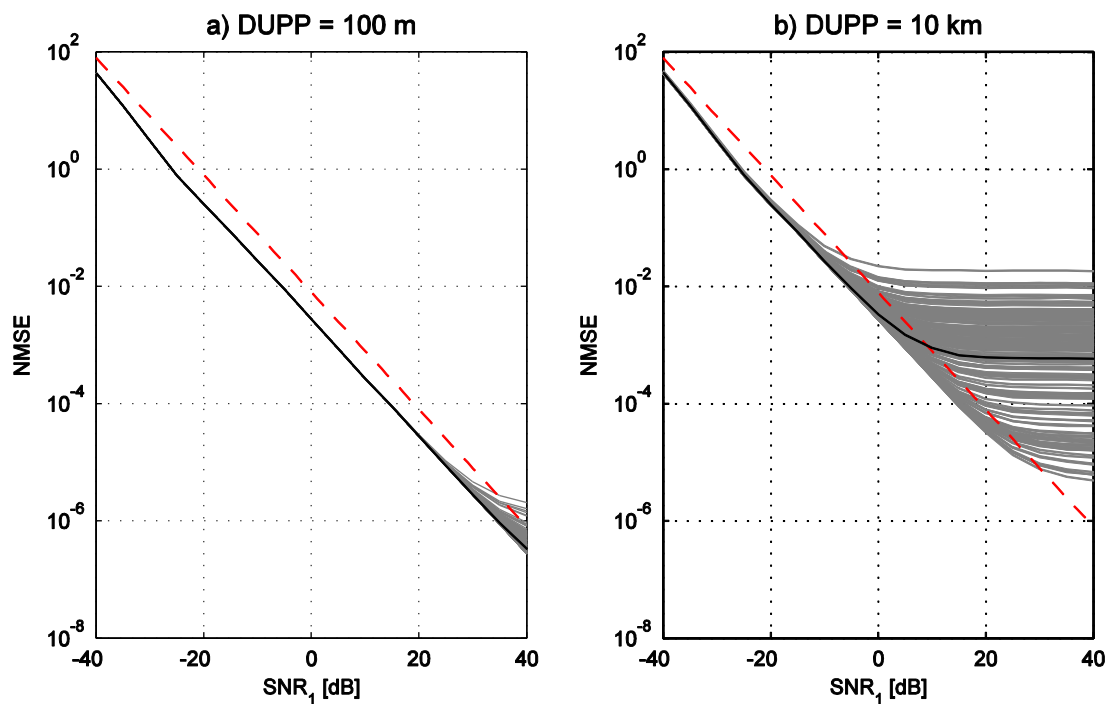
Figure 3.13: Estimation performance in terms of the amplitude NMSE using quasi-orthogonal and linearly dependent unique words at given DUPP

3.5   Conclusion

State of the art technologies for channel estimation on multibeam satellite forward links try to minimize the interference. The developed LAUCO method follows a significantly different way of thinking. It tackles the detrimental interference, which has deterministic origins, in a novel way by construction of a unique word exploiting the knowledge of the user terminal position and the antenna model. The idea behind that approach is to change the role of the interference in the system from a detrimental noise to a helpful signal. Performance figures for the provided system reveal that LAUCO performs significantly better than current technologies and that it is quite robust against inaccurate knowledge of the user position.

The superior performance of LAUCO, compared to state-of-the-art technologies, was recognized by Graz University of Technology and a patent filing process was triggered.

4   Summary

Efficient information transfer is the Holy Grail in the realm of communications, which especially holds true for wireless systems since licensed bandwidth is expensive. To exploit the latter efficiently, accurate knowledge about the current link conditions is mandatory demanding accurate parameter estimation methods which were discussed for mobile satellite channels and multibeam satellite links as an extension of the work presented in [1].

Mobile satellite links were modelled as Rice channels in Chapter 2. According to recent advances in [7] and [8], a broad theoretical analysis was presented, delivering two maximum likelihood estimators for the power parameters and power ratios presuming knowledge of the Doppler spread and the angle of signal arrival. Therefore a suitable DA estimator for frequency estimation and correction was applied ahead, followed by a carrier phase recovery. An appropriate Doppler spread estimator delivering the Doppler spread and hence the region in the periodogram occupied by noise power only was the next step. From there the power estimates and their respective ratios were established and compared for both estimators. The nonlinear (NL) and more complex method improved the estimation performance of only the Rice factor (signal-to-interference ratio) within a limited signal-to noise-ratio region compared to the simplified estimator (HE); this fact and its higher complexity as well as the required knowledge about the channel spectral shape suggest to resort to the HE method for most practical implementations. The presented analyses also holds true for general mobile links following a Rayleigh distribution with line-of-sight component.

Multibeam satellite links are of major concern of current research activities as they are an enabler technology to boost the throughput in the coverage region of a satellite at no extra cost for licensed bandwidth. Given aggressive frequency reuse strategies, interference is a major hurdle to tackle; algorithms mitigating the latter again require accurate channel estimations. For the latter this thesis presented and analysed an estimation concept which employs the knowledge of the user terminal position and the multibeam antenna pattern in a novel way, i.e. the method tackles the detrimental interference, which has deterministic origins, by construction of a unique word based on the knowledge of the user terminal position and the antenna model. The idea behind that approach is to change the role of the interference in the system from a detrimental noise to a helpful signal. Performance figures for the provided system and performance comparisons to

state-of-the-art methods reveal that the invented method performs significantly better than current technologies and that it is quite robust against inaccurate knowledge of the user position. Based on these analyses, Graz University of Technology decided to preserve all rights of use for this technology and triggered a patent filing.

5   Future Outlook

Although the investigated topics are vast and interesting topics for future research are manifold, the author wishes to provide some problem formulations which could provide appropriate entry points for follow-up research. The problem formulations are stated as bullet points and make no claim to be complete.

- *Doppler spread estimation*: Current Doppler spread estimators well operate at angles of arrival of 90°; however, to the best of the authors knowledge, no estimators are available from the open literature, which are able to perform well at arbitrary incidence angles. A promising entry point could be an extension of the idea behind the HDS estimator described in [6]. From there a performance analysis of the complete estimation framework should be performed.

- *Practical Demonstration of the LAUCO estimation concept:* A practical implementation and demonstration of the LAUCO estimation on multibeam channels should be performed. In that context, the Institute of Communication Networks and Satellite Communications of Graz University of Technology is about to set up a demonstrator platform to validate the concept.

- *LAUCO technology exploitation and worldwide patent:* After having practically demonstrated the LAUCO concept, business concepts should be fostered. Currently the patent was filed in Austria only; since this technology is of global interest, an international PCT patent filing should be targeted by the stakeholders.

REFERENCES

[1]   M. Bergmann. "Parameter Estimation on Interference-Imposed Satellite Channels", Dissertation, Graz University of Technology, Austria, 2012.

[2]   E. A. Candreva et al. "SatNEx III, CoO2-Task 3: Flexible and High Performance Adaptive Modulation and Coding Techniques for Satellite Multimedia Applications; TN 3.2 Initial Results", ESA Technical Note, Contract No. 23089/10/NL/CLP, Oct. 2011.

[3]   R. Baroni et al. "SatNEx III, CoO2-Task 3: Flexible and High Performance Adaptive Modulation and Coding Techniques for Satellite Multimedia Applications; Executive Summary Report", ESA Final Report, Contract No. 23089/10/NL/CLP, June 2012.

[4]   R. Baroni et al. "SatNEx III, CoO2-Task 3: Flexible and High Performance Adaptive Modulation and Coding Techniques for Satellite Multimedia Applications; Summary Report", ESA Final Report, Contract No. 23089/10/NL/CLP, June 2012.

[5]   R. Baroni et al. "SatNEx III, CoO2-Task 3: Flexible and High Performance Adaptive Modulation and Coding Techniques for Satellite Multimedia Applications; Final Report", ESA Final Report, Contract No. 23089/10/NL/CLP, June 2012.

[6]   W. Gappmair, M. Bergmann, and O. Koudelka. "Estimation of Carrier and Channel Parameters for Land Mobile Satellite Links", in *Proc. IEEE 6th Advanced Satellite Mobile Syst. Conf.*, Baiona, Spain, pp. 328-334, Sept. 2012.

[7]   W. Gappmair. "Estimation of Carrier and Power Parameters in Time-Selective Fading Channels", Internal Document, Institute of Communication Networks and Satellite Communications, Graz University of Technology, 2013.

[8]   W. Gappmair and M. Bergmann. "Estimation of Carrier and Power Parameters in Time-Selective Fading Channels", *to be submitted to IEEE Commun. Lett*.

[9]   U. Mengali and A. N. D'Andrea. *Synchronization Techniques in Digital Receivers*, New York, NY: Plenum Press, 1997.

[10]   W. Gappmair. "Cramer-Rao Bounds for Joint Parameter Estimation in Correlated Ricean Channels", Internal Document, Institute of Communication Networks and Satellite Communications, Graz University of Technology, Austria, 2011.

[11]   E. A. Candreva et al. "SatNEx III, CoO2-Task 3: Flexible and High Performance Adaptive Modulation and Coding Techniques for Satellite Multimedia

Applications; TN 3.1 State of the art review and consolidation of system specifications", ESA Technical Note, Contract No. 23089/10/NL/CLP, Sept. 2011.

[12] A. J. Goldsmith and P. P. Varaiya. "Capacity of Fading Channels with Channel Side Information", *IEEE Trans. Inform. Theory*, vol. 43, no. 6, pp. 1986 – 1992, Nov. 1997.

[13] S. Cioni, R. De Gaudenzi, and R. Rinaldo. "Channel estimation and physical layer adaptation techniques for satellite networks exploiting adaptive coding and modulation", *Int. J. Satellite Commun. Network.,* vol. 26, pp. 157–188, March/April 2008.

[14] S. Vassaki, A. D. Panagopoulos, and P. Constantinou. "Effective capacity and optimal power allocation for mobile satellite systems and services", *IEEE Commun. Lett.*, vol. 16, pp. 60–63, Jan. 2012.

[15] D. Tarchi, G. E. Corazza, and A. Vanelli-Coralli. "Adaptive coding and modulation techniques for mobile satellite communications: a state estimation approach", in *Proc. IEEE 6th Advanced Satellite Mobile Syst. Conf.*, Baiona, Spain, Baiona, Spain, pp. 36–43, Sept. 2012.

[16] S. O. Rice. "Statistical properties of a sine wave plus random noise", *Bell Syst. Tech. J.*, vol. 27, pp.109-157, Jan. 1948.

[17] M. J. Gans. "A Power-Spectral Theory of Propagation in the Mobile-Radio Environment", *IEEE Trans. Vehicular Technol.*, vol. 21, no. 1, pp. 27-38, Feb. 1972.

[18] R. H. Clarke. "A Statistical Theory of Mobile-Radio Reception", *Bell Syst. Tech. J.*, pp. 957-1000, Jul.-Aug. 1968.

[19] M. K. Simon and M.-S. Alouini. *Digital Communications over Fading Channels: A Unified Approach to Performance Analysis*. New York, NY: John Wiley & Sons, 2000.

[20] F. Gini, M. Luise, and R. Reggiannini. "Cramer-Rao Bounds in the Parametric Estimation of Fading Radiotransmission Channels", *IEEE Trans. Commun.*, vol. 46, no. 10, pp. 1390-1398, Oct. 1998.

[21] U. Mengali and M. Morelli. "Data-Aided Frequency Estimation for Burst Digital Transmission", *IEEE Trans. Commun.*, vol. 43, no. 2/3/4, Feb./Mar./Apr., 1995.

[22] M. Luise and R. Reggiannini. "Carrier Frequency Recovery in All-Digital Modems for Burst Mode Transmissions", in *IEEE Trans. Commun.*, vol. 45, no. 1, pp. 23-25, Jan., 1997.

[23] D. C. Rife and R. R. Boorstyn. "Single-Tone Parameter Estimation from Discrete-Time Observations", *IEEE Trans. Info. Theory*, vol. 20, no. 5, pp. 591-598, Sep. 1974.

[24] A. Papoulis. *Probability, Random Variables, and Stochastic Processes*, Mc Graw Hill: New York, 1991.

[25] W. H. Press, S. A. Teukolsky, W. T. Vetterling and B. P. Flannery. *Numerical Recipes in C: The Art of Scientific Computing*, Cambridge Univ. Press: New York, 1994.

[26] K. E. Baddour and N. C. Beaulieu. "Nonparametric Doppler Spread Estimation for Flat Fading Channels", in *Proc. IEEE Wireless Commun. and Networking Conf.*, New Orleans, LA, USA, pp. 953-958, May 2003.

[27] K. E. Baddour and N. C. Beaulieu. "Robust Doppler Spread Estimation in Nonisotropic Fading Channels", *IEEE Trans. Wireless Commun.*, vol. 4, no. 6, pp. 2677–2682, Nov. 2005.

[28] C. Woodford and C. Philips. *Numerical Methods with Worked Examples*, 1st ed., London (UK): Chapman & Hall, 1997.

[29] B. Dasgupta. *Applied Mathematical Methods*, 2nd ed., Delhi (India): Dorling Kindersley, 2007.

[30] M. Bergmann, W. Gappmair, B. Süsser-Rechberger. "Location-Aware Unique Word Construction for Interference-Free Channel Estimation on Multibeam Satellite Links", Internal Document, Institute of Communication Networks and Satellite Communications, Graz University of Technology, July 2013.

[31] H.-J. Bartsch. *Taschenbuch Mathematischer Formeln*, 19th ed., Chemnitz (Germany): Fachbuchverlag Leipzig, 2001.

[32] G. Gallinaro. "Novel Intra-System Interference Mitigation Techniques & Technologies for Next Generations Broadband Satellite Systems: Executive Summary Report", ESA Final Report, Contract No. 18070/04/NL/US, Feb. 2008.

[33] F. Lombardo et al. "SatNEx III, CoO1 Task 2: Hybrid Space Ground Processing; Internal TN on Antenna Model Analysis", ESA Technical Note, Contract No. RFQ/3-12859/09/NL/CLP, June 2010.

[34] P. Angeletti, G. Gallinaro, M. Lisi, and A. Vernucci. "On-Ground Digital Beamforming Techniques for Satellite Smart Antennas", in *Proc. 19th AIAA*, Toulouse, France, pp. 1–8, April 2001.

[35] P. Angeletti and N. Alagha. "Space/Ground Beamforming Techniques for Emerging Hybrid Satellite Terrestrial Networks", in *Proc. 27th AIAA*, Edinburgh, UK, pp. 1–6, June 2009.

[36] B. Devillers et al. "SatNEx III, CoO1 Task 2: Hybrid Space Ground Processing; TN 2.1 DigiSat Techniques Review", ESA Technical Note, Contract No. RFQ/3-12859/09/NL/CLP, June 2010.

[37] B. Devillers et al. "SatNEx III, CoO1 Task 2: Hybrid Space Ground Processing; TN 2.3 DigiSat Techniques Pre-Selection", ESA Technical Note, Contract No. RFQ/3-12859/09/NL/CLP, Nov. 2010.

[38] B. Devillers et al. "SatNEx III, CoO1 Task 2: Hybrid Space Ground Processing; TN 2.4 Digisat Analysis and Trade-Offs", ESA Technical Note, Contract No. RFQ/3-12859/09/NL/CLP, Nov. 2010.

[39] B. Devillers et al. "SatNEx III, CoO1 Task 2: Hybrid Space Ground Processing; TN 2.5 Digisat Recommendations and Roadmap", ESA Technical Note, Contract No. RFQ/3-12859/09/NL/CLP, Nov 2010.

[40] B. Devillers et al. "SatNEx III, CoO1 Task 2: Hybrid Space Ground Processing; Final Report", ESA Technical Note, Contract No. RFQ/3-12859/09/NL/CLP, May 2011.

[41] B. Devillers et al. "SatNEx III, CoO1 Task 2: Hybrid Space Ground Processing; Summary Report", ESA Contract No. RFQ/3-12859/09/NL/CLP, May 2011.

[42] M. Bergmann, W. Gappmair, C. Mosquera and O. Koudelka. "Channel Estimation on the Forward Link of Multi-Beam Satellite Systems", in *Proc. 3rd Int. ICST Conf. on Personal Satellite Service* (PSATS), Malaga, Spain, pp. 1–10, Feb. 2011.

[43] J. Arnau-Yanez, M. Bergmann, E. A. Candreva, G. E. Corazza, R. De Gaudenzi, B. Devillers, W. Gappmair, F. Lombardo, C. Mosquera, A. Perez-Neira, I. Thibault, and A. Vanelli-Coralli. "Hybrid Space-Ground Processing for High-Capacity Multi-beam Satellite Systems", in *IEEE Global Telecommun. Conf.* (GLOBECOM), Houston/TX, pp.1–6, Dec. 2011.

[44] M. Bergmann, W. Gappmair, B. Süsser-Rechberger, and O. Koudelka. "Location Aware Channel Estimation for Capacity Gains on MIMO Satellite Links", in *Proc. 63rd Int. Astronautical Federation Congress*, IAC-12-B2.4.7, pp. 1–5, Sept. 2012.

[45] M. Bergmann, W. Gappmair, B. Süsser-Rechberger, and O. Koudelka. "Location Aware Channel Estimation for Capacity Gains on Multibeam Satellite Links", *Acta Astronautica*, vol. 91, pp. 131–136, 2013.

[46] B. Süsser-Rechberger. "Position-based channel estimation on MIMO satellite forward links", B.Sc. Thesis, Graz University of Technology, Austria, 2012.

ABBREVIATIONS

ACM	Adaptive Coding and Modulation
AoA	Angle of Arrival
AWGN	Additive White Gaussian Noise
CRLB	Cramer-Rao Lower Bound
CSI	Channel State Information
DA	Data-Aided
DFT	Discrete Fourier Transform
DUPP	Dilution of User Positioning Precision
ESA	European Space Agency
FIR	Finite Impulse Response
HE	Heuristic Estimation
IKS	Institute for Communication Networks and Satellite Communications
LACE	Location-Aware Channel Estimation
LAUCO	Location-Aware Unique Word Construction
LLF	Log-Likelihood Function
LoS	Line-Of-Sight
LPF	Low-Pass Filter
MCRLB	Modified Cramer-Rao Lower Bound
MEV	Mean Estimator Value
ML	Maximum Likelihood
MSE	Mean Square Error
NCRLB	Normalized CRLB
NMEV	Normalized MEV
NMSE	Normalized MSE
NL	Non-Linear
NTV	Normalized True Value
PSD	Power Spectral Density
QPSK	Quadrature Phase Shift Keying
RTT	Round-Trip Time
Rx	Receiver
SIR	Signal-to-Interference Ratio
SNIR	Signal-to-Noise-plus-Interference Ratio
SNR	Signal-to-Noise Ratio

| Tx | Transmitter |
| UT | User Terminal |